UNIVERSITY OF WEST ATTICA
SCHOOL OF ENGINEERING
DEPARTMENT OF MECHANICAL ENGINEERING

DIPLOMA THESIS

«Numerical study of rarefied gas flows in micro propulsion nozzles using the stochastic DSMC method»

Litovoli Foteini (R.N.: 18392023)

Supervisors:
Dr. Sarris Ioannis
Dr. Tantos Christos

Athens, March 2024

ΠΑΝΕΠΙΣΤΗΜΙΟ ΔΥΤΙΚΗΣ ΑΤΤΙΚΗΣ
ΣΧΟΛΗ ΜΗΧΑΝΙΚΩΝ
ΤΜΗΜΑ ΜΗΧΑΝΟΛΟΓΩΝ ΜΗΧΑΝΙΚΩΝ

ΔΙΠΛΩΜΑΤΙΚΗ ΕΡΓΑΣΙΑ

« Αριθμητική μελέτη ροών σε ακροφύσια μικροπροωθητήρων με χρήση της στοχαστικής μεθόδου DSMC»

Λιτοβολή Φωτεινή (Α.Μ.: 18392023)

Επιβλέπων Καθηγητές:
Δρ. Σαρρής Ιωάννης
Δρ. Τάντος Χρήστος

Αθήνα, Μάρτιος 2024

ΠΑΝΕΠΙΣΤΗΜΙΟ ΔΥΤΙΚΗΣ ΑΤΤΙΚΗΣ

ΣΧΟΛΗ ΜΗΧΑΝΙΚΩΝ

ΤΜΗΜΑ ΜΗΧΑΝΟΛΟΓΩΝ ΜΗΧΑΝΙΚΩΝ

«Numerical study of rarefied gas flows in micro propulsion nozzles using the stochastic DSMC method»

Η διπλωματική εργασία βαθμολογήθηκε και έγινε αποδεκτή από την εξής επιτροπή:

Μέλη Εξεταστικής Επιτροπής

Α/Α	ΟΝΟΜΑ/ΕΠΩΝΥΜΟ	ΒΑΘΜΙΔΑ/ΙΔΙΟΤΗΤΑ	ΨΗΦΙΑΚΗ ΥΠΟΓΡΑΦΗ
1	ΙΩΑΝΝΗΣ ΣΑΡΡΗΣ	ΚΑΘΗΓΗΤΗΣ	Ioannis Sarris Digitally signed by Ioannis Sarris Date: 2024.04.22 18:11:04 +03'00'
2	ΚΑΡΒΕΛΑΣ ΕΥΑΓΓΕΛΟΣ	Ε.Ε.Π.	Evangelos Karvelas Digitally signed by Evangelos Karvelas Date: 2024.04.21 15:35:56 +03'00'
3	ΓΕΩΡΓΙΟΣ ΣΟΦΙΑΔΗΣ	Ε.ΔΙ.Π.	GEORGIOS SOFIADIS Digitally signed by GEORGIOS SOFIADIS Date: 2024.04.19 12:36:03 +03'00'

ΔΗΛΩΣΗ ΣΥΓΓΡΑΦΕΑ ΔΙΠΛΩΜΑΤΙΚΗΣ ΕΡΓΑΣΙΑΣ

Η κάτωθι υπογεγραμμένη Λιτοβολή Φωτεινή του Πέτρου, με αριθμό μητρώου 18392023 φοιτήτρια του Πανεπιστημίου Δυτικής Αττικής της Σχολής Μηχανικών του Τμήματος Μηχανολόγων Μηχανικών, δηλώνω υπεύθυνα ότι:

«Είμαι συγγραφέας αυτής της διπλωματικής εργασίας και ότι κάθε βοήθεια την οποία είχα για την προετοιμασία της είναι πλήρως αναγνωρισμένη και αναφέρεται στην εργασία. Επίσης, οι όποιες πηγές από τις οποίες έκανα χρήση δεδομένων, ιδεών ή λέξεων, είτε ακριβώς είτε παραφρασμένες, αναφέρονται στο σύνολό τους, με πλήρη αναφορά στους συγγραφείς, τον εκδοτικό οίκο ή το περιοδικό, συμπεριλαμβανομένων και των πηγών που ενδεχομένως χρησιμοποιήθηκαν από το διαδίκτυο. Επίσης, βεβαιώνω ότι αυτή η εργασία έχει συγγραφεί από μένα αποκλειστικά και αποτελεί προϊόν πνευματικής ιδιοκτησίας τόσο δικής μου, όσο και του Ιδρύματος. Παράβαση της ανωτέρω ακαδημαϊκής μου ευθύνης αποτελεί ουσιώδη λόγο για την ανάκληση του διπλώματός μου.»

Η δηλούσα

Φωτεινή Λιτοβολή

Λιτοβολή Φωτεινή

Abstract

Micro propulsion systems are a very important part of modern technology. They can be nuclear powered ones, laser-thermal, solar thermal propelled, or electric ones and all make use of a chamber along with a nozzle. Micro-propulsion systems can be used in medicine micro-bots, underwater vehicles, microsatellites or in the space industry. Under the conditions met in the micro propulsion systems, the flow through the nozzle covers the whole range of the gas collisionality and the gas behaviour cannot be captured by the usual Navier-Stokes formulation (compressible or not). Instead, the gas flow behaviour in these systems should be studied at the molecular level based on the kinetic theory of gases. In this thesis, non-equilibrium transport phenomena appearing in the flows through micro-nozzles will be studied at the microscopic level via the kinetic theory of gases. The stochastic method Direct simulation Monet Carlo (DSMC) will be applied and the validity of the provided results will be demonstrated by performing comparisons with available theoretical/experimental data. Overall, the thesis will provide an analysis of the micro propulsion nozzle performance paying special attention on the study of the influence of the implicit boundary conditions. Some conclusions useful in the numerical simulation of the micro propulsion nozzles will be drawn.

Keywords: rarefied gas, nozzles, DSMC, implicit boundary conditions, stochastic method

Περίληψη

Τα συστήματα μικρο-προώθησης αποτελούν ένα πολύ σημαντικό μέρος της σύγχρονης τεχνολογίας. Μπορεί να είναι πυρηνικά, λέιζερ-θερμικά, ηλιακά θερμικά προωθούμενα ή ηλεκτρικά και όλα κάνουν χρήση ενός θαλάμου μαζί με ένα ακροφύσιο. Τα συστήματα μικρο-προώθησης μπορούν να χρησιμοποιηθούν σε μικρο-ρομπότ της ιατρικής, υποβρύχια οχήματα, μικρο-δορυφόρους ή στη διαστημική βιομηχανία. Υπό τις συνθήκες που πληρούνται στα συστήματα μικροπροώθησης, η ροή μέσω του ακροφυσίου καλύπτει όλο το εύρος της αραιοποίησης του αερίου και η συμπεριφορά του αερίου δεν μπορεί να περιγραφεί από τη συνήθη θεωρία Navier-Stokes (συμπιεστή ή μη). Αντίθετα, η συμπεριφορά της ροής αερίων σε αυτά τα συστήματα θα πρέπει να μελετηθεί σε μοριακό επίπεδο με βάση την κινητική θεωρία των αερίων. Σε αυτή τη διπλωματική εργασία θα μελετηθούν σε μικροσκοπικό επίπεδο φαινόμενα μεταφοράς μη ισορροπίας που εμφανίζονται στις ροές μέσω μικρο-ακροφυσίων με χρήση της κινητικής θεωρίας των αερίων. Θα εφαρμοστεί η στοχαστική μέθοδος Άμεσης προσομοίωσης Monte Carlo (DSMC) και η εγκυρότητα των παρεχόμενων αποτελεσμάτων θα εξετασθεί πραγματοποιώντας συγκρίσεις με διαθέσιμα θεωρητικά/πειραματικά δεδομένα. Συνολικά, η διπλωματική θα παρέχει μια ανάλυση της απόδοσης των συστημάτων προώθησης δίνοντας ιδιαίτερη έμφαση στη μελέτη της επίδρασης των οριακών συνθηκών. Θα εξαχθούν χρήσιμα συμπεράσματα για την υπολογιστική προσομοίωση των ακροφυσίων των συστημάτων μικροπροώθησης.

Λέξεις Κλειδιά: αραιωποιημένο αέριο, ακροφύσια, DSMC, implicit boundary conditions, στοχαστική μέθοδος

Acknowledgements

I want to express my deep appreciation for the invaluable support and guidance provided by Dr Christos Tantos, throughout the course of this thesis. His patience and dedication in sharing knowledge not only contributed to enhancing my understanding of intricate concepts, but also created a conducive environment where I could learn and develop comfortably without feeling inadequate due to any lack of expertise.

I am grateful to Dr Ioannis Sarris as I owe the initiation of this thesis to him. He showed openness in considering my thoughts and dedicated time to identify the most suitable option for me. I would also like to acknowledge Giorgos Sofiadis for his support and kindness. He always welcomed me with a helping hand and a friendly demeanour, contributing to the positive atmosphere of my thesis experience.

My deepest gratitude extends to my friends who have shown remarkable understanding, when I was unable to meet them for a prolonged duration, and being always available despite their own challenges.

Finally, I owe an immeasurable debt of gratitude to my family whose steadfast support formed the foundation upon which I could pursue this thesis. Their encouragement and love have been an unending source of motivation that I deeply appreciate.

Contents

Abstract v
Περίληψη vi
Acknowledgements vii
Table of Figures x
1. Chapter 1: Introduction 1
1.1 Propulsion Systems 1
1.2 Fundamentals of rocket propulsion Systems 2
1.3 Thesis Scopus 3
2. Chapter 2: Kinetic Theory 5
2.1 Knudsen number and flow regimes 5
2.2 Mach and Reynolds number 6
2.3 Boltzmann equation 8
2.4 Boundary conditions 9
2.5 Numerical methods 11
3. Chapter 3: DSMC Method 13
3.1 Introduction 13
3.2 Main Steps of the DSMC Algorithm 13
3.3 Molecular Description 14
3.4 Random number 15
3.5 Collisions 15
3.6 Macroscopic quantities 16
3.7 Boundary conditions 17
3.8 Description of the model problem 18
3.9 Results of the model problem and sensitivity of the method 18
4. Chapter 4: Numerical Analysis of Nozzle Performance 23
4.1 Propulsion Nozzles 23
4.2 Flow Configuration 25
4.3 Implicit Boundary Conditions 26
4.4 Fully Developed method 27
4.5 Complete Solution 29
4.6 Parametric Study and Benchmarking 29
4.6.1 Parametric Analysis 29
4.6.2 Comparison with available data in literature on diverging channel 30
4.6.3 Comparison with available data in literature on straight channel 31

4.7 Results and Discussion 32
4.7.1 Mass flow rate 32
4.7.2 Thrust and Impulse factor 34
4.7.3 Contours of Dimensionless Density, Temperature and Velocity 37
4.7.4 Axial Distributions of Density, Temperature and Velocity 42
4.7.5 Distributions of Density, Temperature and Velocity along the y-axis .. 46
4.7.6 Mach, Knudsen and Reynolds numbers 50
5. Chapter 5: Conclusions and Future work 53
5.1 Conclusions 53
5.2 Future Work 53
6. Bibliography 54
7. Appendix 58
7.1 Appendix A: Complete Solution with DVM 58

Table of Figures

Figure 2.1: Flow regimes and equations [12]. 6
Figure 3.1: The standard DSMC procedure [30]. 14
Figure 3.2: Model problem set up. 18
Figure 3.3: Graphs of heat flux vs time for different values of Δx. 20
Figure 3.4: Graphs of heat flux vs time for different values of particles. 21
Figure 3.5: Diagram of heat flux to time for δ=1.5, β=0.5, particles=8000 and cells=400 for different timestep. 22
Figure 4.1: Flow configuration set up. 26
Figure 4.2:Density contours for $PR = 0.1$ (a, b, c, d, e, f, g, h) and $PR = 0.5$ (i, j, k, l, m, n, o, p), for $\delta = 1$ (a, b, c, d, I, j ,k, l) and $\delta = 10$ (e, f, g, h, m, n, o, p), for $LHin$=5 (a, c, e, g, i, k, m, o) and $LHin = 10$ (b, d, f, h, j, l, n, p), for $HoutHin = 2$ (a, b, e, f, i, j, m, n) and $HoutHin =$ (c, d, g, h, k, l, o, p). 39
Figure 4.3: Temperature contours for $PR = 0.1$ (a, b, c, d, e, f, g, h) and $PR = 0.5$ (i, j, k, l, m, n, o, p), for $\delta = 1$ (a, b, c, d, I, j ,k, l) and $\delta = 10$ (e, f, g, h, m, n, o, p), for L/H_1=5 (a, c, e, g, i, k, m, o) and $LHin = 10$ (b, d, f, h, j, l, n, p), for $HoutHin = 2$ (a, b, e, f, i, j, m, n) and $HoutHin = 5$ (c, d, g, h, k, l, o, p). 40
Figure 4.4: Velocity contours for $PR = 0.1$ (a, b, c, d, e, f, g, h) and $PR = 0.5$ (i, j, k, l, m, n, o, p), for $\delta = 1$ (a, b, c, d, I, j ,k, l) and $\delta = 10$ (e, f, g, h, m, n, o, p), for $LHin = 5$ (a, c, e, g, i, k, m, o) and $LHin = 10$ (b, d, f, h, j, l, n, p), for $HoutHin = 2$ (a, b, e, f, i, j, m, n) and $HoutHin = 5$ (c, d, g, h, k, l, o, p). 41
Figure 4.5: Axial distributions of density for $PR = 0.1$ (a, b, c, d) and $PR = 0.5$ (e, f, g , h), for $LHin = 10$ (a, b, e, f) and $LHin = 10$ (c, d, g, h), for $HoutHin = 2$ (a, c, e, g) and $HoutHin = 5$ (b, d, f, h). 43
Figure 4.6: Axial distributions of temperature for $PR = 0.1$ (a, b, c, d) and $PR = 0.5$ (e, f, g , h), for $LHin = 5$ (a, b, e, f) and $LHin = 10$ (c, d, g, h), for $HoutHin = \mathbf{2}$ (a, c, e, g) and $HoutHin = 5$ (b, d, f, h). 44
Figure 4.7: Axial distributions of velocity for $PR = 0.1$ (a, b, c, d) and $PR = 0.5$ (e, f, g , h), for $LHin = 5$ (a, b, e, f) and $LHin = 10$ (c, d, g, h), for $HoutHin = 2$ (a, c, e, g) and $HoutHin = 5$ (b, d, f, h). 45
Figure 4.8: Perpendicular distributions of density for $PR = 0.1$ (a, b, c, d) and $PR = 0.5$ (e, f, g , h), for $LHin = 5$ (a, b, e, f) and $LHin = 10$ (c, d, g, h), for $HoutHin = 2$ (a, c, e, g) and $HoutHin = 5$ (b, d, f, h). 47
Figure 4.9: Perpendicular distributions of velocity for $PR = 0.1$ (a, b, c, d) and $PR = 0.5$ (e, f, g , h), for $LHin = 5$ (a, b, e, f) and $LHin = 10$ (c, d, g, h), for $HoutHin = 2$ (a, c, e, g) and $HoutHin$=5 (b, d, f, h). 48
Figure 4.10: Perpendicular distributions of temperature for $PR = 0.1$ (a, b, c, d) and $PR = 0.5$ (e, f, g , h), for $LHin = 5$ (a, b, e, f) and $LHin = 10$ (c, d, g, h), for $HoutHin$ =2 (a, c, e, g) and $HoutHin$ =5 (b, d, f, h). 49

Αφιερωμένο στους γονείς μου

1. Chapter 1: Introduction

1.1 Propulsion Systems

Micro-spacecrafts' implication includes the necessity for small systems. Early satellites, such as Explorer I and Vanguard I, were limited in size due to constraints with early launch vehicles and lacked truly miniature systems, resulting in limited functionality. Over time, technological advancements led to the development of more complex satellite capabilities including pointing requirements and precise orbit maintenance. Propulsion systems were then integrated onboard to counteract various disturbances and gravitational effects caused by the Earth's oblateness [1].

Rocket propulsion systems can be categorized in various ways. Based on the type of energy source there are chemical, nuclear, or solar propulsion systems. In addition, they can be categorised based on their primary function (including booster stage, sustainer and upper stages, attitude control, orbit station keeping). They can also be classified according to the vehicle they propel like aircraft, missile and assisted take off vehicles. Other ways to categorize rocket propulsion systems is by considering their size, propellant type and construction materials. Additionally, rockets may be classified by the number of propulsion units used in a particular vehicle. A useful approach for categorization is considering how thrust is produced. Most common rocket propulsion systems rely on utilizing the thermodynamic expansion of gas in a supersonic nozzle. This process involves converting internal energy of the propellant into exhaust kinetic energy while generating thrust from pressure exerted on surfaces exposed to exhaust gases. The same principle and equipment are employed across various types of propulsion systems including jet propulsion, nuclear powered ones, laser-thermal, solar thermal propelled, and certain varieties of electrical spacecrafts which all make use of a chamber along with a nozzle [2].

Electric and non-electric propulsion systems are distinguished by their reliance on electrical power. Electric propulsion systems need a continuous supply of electricity to function, while non-electric or chemical propulsion systems may only need small amounts of power at the beginning and end of operation[3]. Electric propulsion has been appealing due to its relatively high performance, generating the required amount of thrust with moderate propellant usage. However, existing electrical power supplies limit it to relatively low thrust levels. In contrast to chemical propulsion, electric propulsion uses energy sources (such as nuclear, solar radiation, or batteries) that are separate from the propellant being used. To achieve substantial increases in vehicle velocity, low thrusts must be applied for significantly longer durations compared to chemical propulsion, sometimes lasting for months or even years [2].

Resistojet thrusters fall under the category of electro-thermal engines, which can function effectively at both high and low power levels, depending on their design and

the specific requirements of the mission [4]. Resistojets function by circulating the propellant in its gaseous form around an electric heater to elevate its temperature. This process enables the use of a conventional convergent-divergent nozzle to propel the propellant to supersonic speeds and generate thrust. The heating can occur through direct contact between the heating element and the propellant, or indirectly when surrounding elements heat the thruster case. Heating the propellant reduces gas flow rate at a given upstream pressure and nozzle area [5].

High-power resistojets operate within a range of 0.5 to 1.5 kWatt with a specific impulse of 300 to 350 s using propellants such as Hydrazine or Ammonia. These engines were initially developed in the early 1960s. However, there is currently a greater focus on low-power systems due to increased interest in smaller satellites. Low-power systems can operate below 100 W while producing thrust up to100 mN with a specific impulse of up to 100 s based on the propellant [5].

1.2 **Fundamentals of rocket propulsion Systems**

A very important factor of rocket propulsion systems is thrust. Thrust is the force generated by the rocket's propulsion system, acting at the centre of mass of the vehicle. It is a reactive force experienced by the structure of the vehicle due to propellant being expelled at high speeds. Momentum, a vector quantity, is defined as the product of an object's mass and its velocity vector. In rocket propulsion, small amounts of propellant are expelled from within the vehicle at high velocities.

The thrust F_m (N), due to a change in momentum, is shown below in equation 1.1. The relationship between thrust and change in momentum assumes constant exit gas velocity and uniform axial flow when there is a constant mass flow rate. Idealized thrust can closely approximate actual thrust but only represents total propulsive force when nozzle exit pressure equals ambient pressure.

$$F_m = \frac{d(Mu_{out})}{dt} = \dot{M}u_{out} \tag{1.1}$$

Where $\dot{M}$ the mass flow rate and u_{out} the velocity for the outlet.

Changes in pressure due to altitude variations during flight can lead to imbalances between the exit propellant gas pressure (p_{out}) and the external environment pressure (p_{ex}), for a fixed nozzle geometry. In steady operation within a uniform atmosphere, the total thrust can be demonstrated to be equal to:

$$F_{tot} = \dot{M}u_{out} + (p_{out} - p_{ex})H_{out} \tag{1.2}$$

Where H_{out} the height of the exit.

The first component is the propulsion force created by the multiplication of the propellant mass flow rate and its exhaust velocity in relation to the vehicle. The following element denotes the thrust generated by pressure, resulting from the multiplication of the cross-sectional area at the nozzle exit (where the exhaust jet departs from the vehicle) and the difference between gas pressure and ambient fluid pressure. In the space of vacuum $p_{ex} = 0$ the total thrust becomes [2]:

$$F_{tot} = \dot{M} u_{out} + p_{out} H_{out} \tag{1.3}$$

Another essential performance parameter for rocket systems is the specific impulse (I_{sp}). A higher I_{sp} (s) results in lower propellant consumption and, therefore, less propellant mass. By increasing specific impulse, it could potentially lead to an increase in payload mass, a reduction in spacecraft mass, or a decrease in launch costs while also extending satellite lifetime. Specific impulse determines how much mass a propulsion system will use in its mission and is defined as [6]:

$$I_{sp} = \frac{F_{tot}}{\dot{M} g} \tag{1.4}$$

Where g is the gravitational acceleration at sea level (9.81 m/s^2).

Finally, another factor affecting the effectiveness of propulsion systems is the discharge coefficient (c_D). The discharge coefficient represents the ratio between actual and theoretical discharges, with the actual discharge being the product of the actual cross-sectional area of the jet and the actual velocity.

The above variables can be determined by analysing the flow within propulsion nozzles and help to improve the performance of rocket propulsion systems.

1.3 **Thesis Scopus**

This thesis enhances the understanding of nozzle dynamics and addresses a crucial aspect that has received limited attention in computational studies thus far. The computational time is quite long for the considered problem using computational techniques based on the particle nature of gases, such as DSMC. The time increases with the increase of the computational space and with the decrease of the rarefaction conditions. For this reason, implicit boundary conditions have been proposed. These boundary conditions make some assumptions which allow to reduce the computational space and consequently the time. This type of boundary conditions has been widely used in the literature for nozzle flow studies. But given the assumptions they are based on, they are expected to break down as the rarefaction increases. A validation of the implicit boundary conditions is therefore required. By carefully analysing the errors related to implicit boundary conditions in DSMC simulations,

this thesis aims to bridge this gap and advance discussions about the precision and dependability of such computational methods within the context of nozzle dynamics.

The main goals of the thesis can be further elaborated in three ways. Initially, the focus is on understanding the complexities and operations inherent in the Direct Simulation Monte Carlo code. Secondly, it involves evaluating specific methods used to simulate numerically gas flows within micro nozzles. Lastly, the overall objective is to offer well-informed and practical suggestions for optimizing micro nozzle system research.

Chapter 2 discusses the kinetic theory with a strong focus on the Boltzmann equation and various methods for its solution. It also examines important parameters such as Knudsen, Mach, and Reynolds that characterize gas flows.

In chapter 3, there is a detailed explanation of the DSMC methodology. The DSMC algorithm is illustrated using an example problem related to heat transfer between parallel plates. The validation of the code takes place comparing its results to those found in existing literature.

Chapter 4 presents a review of studies conducted on micronozzles. In this chapter takes place the description of the main geometry of the problem and its parameters. Also, in chapter 4 the results are presented, which are compared with other two kinetic approaches.

Chapter 5 presents the key findings of this thesis and provides a brief overview of potential future research areas.

2. Chapter 2: Kinetic Theory

2.1 Knudsen number and flow regimes

The rarefaction level of a gas is commonly indicated by the Knudsen number Kn [7], which represents the ratio between the mean free path λ (the average distance that a molecule travels before colliding with another molecule) and the characteristic dimension D

$$Kn = \frac{\lambda}{D} \tag{2.1}$$

while D denotes a characteristic length of the issue or a length scale of macroscopic gradient. For hard sphere molecules, the mean free path travelled between collisions can be expressed as

$$\lambda = \frac{1}{\sqrt{2}\pi d^2 n}, \tag{2.2}$$

Where, d is the molecular diameter and n the number density. For macroscopic quantities the mean free path is written

$$\lambda = \frac{\sqrt{\pi}}{2}\frac{\mu u_0}{P}, \tag{2.3}$$

where, μ is the dynamic viscosity of the gas in temperature T and P is the pressure. The molecular velocity is described as

$$u_0 = \sqrt{\frac{2k_B T}{m}}, \tag{2.4}$$

with, k_B the Boltzmann constant [8–10].

In addition to the Knudsen number the rarefaction parameter δ is also commonly used

$$\delta = \frac{\sqrt{\pi}}{2}\frac{D}{\lambda} = \frac{\sqrt{\pi}}{2}\frac{1}{Kn} \tag{2.5}$$

The continuum regime, described by the Navier-Stokes equation, is widely observed in many important applications due to its prevalence. In this flow regime, particles experience frequent collisions and only travel short distances between collisions. The distribution of the velocities of particles located in any small control volume is naturally a normal distribution, which is referred to as a Maxwellian distribution, centred about the mean velocity and with a variance related to the temperature of the flow. Important deviations from these solutions occur in the slip flow regime for $0.1 > Kn > 0.001$ near solid walls, necessitating modified boundary conditions for momentum and energy transfer at the walls. When the collision frequency decreases, the flow becomes free molecular. The free molecular regime is accurately and efficiently modelled through free-flight (ballistic) molecular models when $Kn > 10$, due to negligible molecule-molecule interactions and dominant molecule-wall interactions. During free molecular flow regimes around satellites and industrial processes, collisions are relatively rare and can be neglected solving the Boltzmann equation. However, in transitional regimes, where $10 > Kn > 0.1$, collisions become prevalent enough to invalidate the free molecular assumption without being frequent enough to force particles to adopt Maxwellian velocity distribution functions [8,11,12].

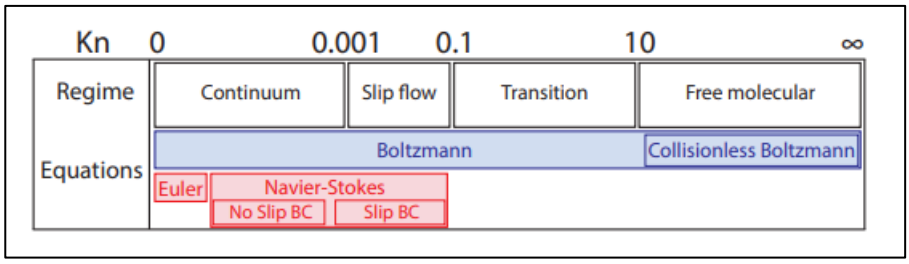

***Figure 2.1**: Flow regimes and equations [12].*

2.2 **Mach and Reynolds number**

The significance of compressibility in the equations of motion can be evaluated by examining the Mach number (Ma), which is defined as the ratio of a representative flow speed to the speed of sound [13].

$$Ma = \frac{u}{c} \tag{2.6}$$

where u is the representative flow speed, and c the speed of sound. Based on the axial bulk velocity u_x the local Ma can be defined as [14]:

$$Ma = \left(\frac{u_x}{u_0}\right)\sqrt{\frac{2T_0}{T\gamma}} \tag{2.7}$$

Where T the local temperature, $\gamma = 5/3$ for monatomic gas.

Based on the Mach number, flows can be generally categorized as follows:

- Incompressible flow: $Ma = 0$. In this case, fluid density remains constant regardless of pressure within the flow field. Although the flowing fluid may technically be a compressible gas, its density is considered to remain unchanged.
- Subsonic flow occurs when the Mach number is between 0 and 1. Shock waves are absent in this type of flow, and in engineering applications, subsonic flows with $Ma < 0.3$ are often considered to be incompressible.
- Transonic flow refers to a range of Mach numbers from 0.8 to 1.2, where shock waves may arise. Analysing transonic flows is challenging due to the nonlinear nature of the governing equations and the difficulty in separating inviscid and viscous aspects of the flow.
- Supersonic flow occurs when the Mach number is greater than 1, leading to the presence of shock waves. Analysing a supersonic flow is often considered easier than analysing subsonic or incompressible flows because information propagates along specific directions known as characteristics, which greatly aids in computing the flow field.
- Hypersonic flow corresponds to Mach greater than 3 and involves very high speeds combined with friction or shock waves that can lead to significant temperature increases in the fluid, causing molecular dissociation and other chemical effects [13].

The Reynolds number holds significant importance in the field of microfluidics as it relates the inertial forces to the viscous forces. The Reynolds number is used to characterize the nature of flow in a channel, such as laminar, turbulent, or critical. It also serves to compute the friction factor in the channel flow. The Reynolds number is dependent on the gas flow rate, the diameter intake, and gas density as well as viscosity.

$$Re = \frac{uDr}{\mu} \tag{2.8}$$

Where Re is the Reynolds number, u the average velocity of gas in channel, D the inside diameter of pipe, r the gas density and μ the gas viscosity.

For tubes with constant cross section laminar flow occurs when the Reynolds number falls below around 2000 while turbulent flow occurs at values surpassing

4000. When the Reynolds numbers range between 2000 and 4000, it results in undefined or critical flow conditions [15,16].

Based on the Ma and Re numbers, the Kn number is defined as:

$$Kn = \frac{Ma}{Re}\sqrt{\frac{\gamma\pi}{2}} \tag{2.9}$$

2.3 **Boltzmann equation**

Simulating gas flows from different regimes traditionally involves employing various methods. The approaches utilized for continuum flows, such as the Navier-Stokes equation solvers in macroscopic fluid dynamics, have been extensively developed. However, these methods present challenges when attempting to seamlessly link computational results across different flow regimes. Current and future engineering developments in spaceflight projects are heavily focused on addressing complex gas dynamic issues related to low-density flows within the intermediate range of Knudsen numbers, particularly in rarefied transition and near-continuum flow regimes. The Boltzmann equation accurately portrays the evolutionary process of the molecular velocity distribution function from non-equilibrium to equilibrium states at any given time within gases. It effectively describes molecular transport phenomena encompassing continuum flow through free-molecular flow regimes [17]. In 1872, L. Boltzmann [18] presented the kinetic equation that governs the change of the distribution function for gaseous systems that are not in equilibrium. The Boltzmann equation applies to dilute gases, in which the existence of exclusively binary collisions between particles can be assumed. In its full form the equation can be written as:

$$\frac{\partial \mathrm{f}}{\partial \mathrm{t}} + \boldsymbol{\xi}\frac{\partial \mathrm{f}}{\partial \mathbf{r}} + \boldsymbol{F}\frac{\partial \mathrm{f}}{\partial \boldsymbol{\xi}} = Q(f, f') \tag{2.10}$$

Where f the distribution function, $\mathbf{r}$ the molecular position, $\boldsymbol{\xi}$ the molecular velocity, Q is the collision operator and $\boldsymbol{F}$ is the acceleration associated with an externally imposed force field.

The Boltzmann equation solution yields the distribution function, which presents the information of the position and molecular velocity of gas molecules over time. The macroscopic properties are derived as moments of this distribution function [9,10].

Number density $$n(t, \boldsymbol{r}) = \int f d\boldsymbol{\xi} \tag{2.11}$$

Velocity vector $$\boldsymbol{u}(t,\boldsymbol{r}) = \frac{1}{n}\int \boldsymbol{\xi} f d\boldsymbol{\xi} \quad (2.12)$$

Pressure $$P(t,\boldsymbol{r}) = \frac{m}{3}\int (\boldsymbol{\xi} - \boldsymbol{u})^2 f d\boldsymbol{\xi} \quad (2.13)$$

Stress tensor $$P_{i,j}(t,\boldsymbol{r}) = m\int (\xi_i - u_i)\left(\xi_j - u_j\right) f d\boldsymbol{\xi} \quad (2.14)$$

Temperature $$T = (t,\boldsymbol{r}) = \frac{m}{3k_B n}\int (\boldsymbol{\xi} - \boldsymbol{u})^2 \, f d\boldsymbol{\xi} \quad (2.15)$$

Heat flux vector $$\boldsymbol{q}(t,\boldsymbol{r}) = \frac{m}{2}\int (\boldsymbol{\xi} - \boldsymbol{u})^2 (\boldsymbol{\xi} - \boldsymbol{u}) f d\boldsymbol{\xi} \quad (2.16)$$

Due to the complexity of the Boltzmann equation, it is difficult directly and exactly to solve the Boltzmann equation. Numerically solving the Boltzmann equation becomes much more manageable by replacing its collision term with dependable kinetic models. The kinetic model equations retain the basic properties of the Boltzmann equation, such as the H-theorem and conservation invariant conditions [17].

The most famous kinetic model is the BGK[19] (by Bhatnagar, Gross and Krook) model for monatomic gases. According to the BGK model, a particle relaxes to the Maxwellian distribution after a single collision. The simplicity of the BGK model has led to its widespread use in literature as it provides accurate results across various Knudsen number ranges. The disadvantage of this model is that it can only be applied to isothermal flows because it does not provides a correct Prandl value [10].

The Shakhov [20] kinetic model, a modification of the BGK model, maintains collision invariants and accurately determines transport coefficients. While proof of its satisfaction of the H-Theorem is limited to its linearized form, it remains widely accepted as a dependable model, consistently yielding precise results across varying flow configurations within different Knudsen number ranges.

Another commonly employed kinetic model is the Ellipsoidal-Statistical model introduced by Holway. This model yields accurate values for the transport coefficients. Nevertheless, it requires greater computational resources compared to the BGK and S models [10].

2.4 **Boundary conditions**

The Boltzmann equation needs to be supplemented by boundary conditions that characterize the interaction between molecules and solid boundaries. The definition of

these boundary conditions serves to connect solid state physics with the kinetic theory of gases.

The earliest gas-surface interaction model in kinetic theory was formulated by J. C. Maxwell [21]. It accounts for two types of interactions: specular and diffuse. A specular interaction, or reflection, occurs when a molecule collides with a solid surface in such a way that it elastically rebounds as if hitting a flat surface. This happens when the gas molecule collides with the peak of the solid's molecular structure, assuming both are hard elastic spheres. The collision results in an inversion of the surface normal component of the molecule's velocity and no change in its tangential component, while maintaining constant thermal energy. On the other hand, a diffuse interaction occurs when an incident molecule attains thermal equilibrium with the solid surface before rebounding from it according to Maxwellian velocity distribution at local temperature. Maxwell's model assumes that some fraction a_M of incident molecules is temporarily absorbed by the surface and then reflected diffusely. All remaining molecules reflect specularly based on this probability a_M. The scattering kernel for this model can be expressed as [22]:

$$K_M\left(\vec{\xi}_i, \vec{\xi}_r\right) = (1 - a_M)\delta\left(\vec{\xi}_i - \vec{\xi}_{r,specular}\right) + a_M f_M\left(\vec{\xi}_r\right)|\vec{\xi}_r \boldsymbol{n}| \qquad (2.17)$$

Where $\vec{\xi}_r$ the reflected molecular velocity, $\vec{\xi}_{r,specular}$ the molecular velocity of specular reflection, f_M the Maxwellian velocity distribution in equilibrium with the solid surface, $\boldsymbol{n}$ local normal of solid surface.

When a stream of molecules is directed towards a surface at a particular angle of incidence, the scattering pattern anticipated by the Maxwell model appears circular due to diffuse reflections and includes a prominent peak resulting from specular reflections. In cases where all molecules in the beam are traveling at identical speeds, the peak forms as a line at the exact reflection angle. However, contrary to what is predicted by the Maxwell model, experimental evidence from molecular beam experiments reveals petal-shaped scattering distributions. These observed patterns are really well explained by the Cercignani and Lampis (CLL) model because of its well-defined interaction parameters, along with its distinct mathematical framework known as scatter kernel construction [22,23]. The CLL model includes two adjustable parameters, specifically the normal energy accommodation coefficient denoted as a_n and the tangential momentum accommodation coefficient denoted as σ_t. The range of a_n is from 0 to 1 and it is associated with the portion of kinetic energy corresponding to the normal velocity. Whereas, σ_t can vary from 0 to 2 and is linked to the tangential momentum [23]. The scattering kernel of this model has the following form:

$$K_{CL}(\vec{\xi}_i, \vec{\xi}_r) = \frac{a_n \sigma_t (2-\sigma_t)^{-1}}{2\pi (R_G T_w^2)} \xi_{n,r} exp(-\frac{\xi_{n,r}^2 (1-a_n) \xi_{n,i}^2}{a_n R_G T_w} - \frac{[\vec{\xi}_{t,r} - (1-\sigma_t)\vec{\xi}_{t,i}]^2}{2\sigma_t (2-\sigma_t) R_G T_w}) I_0(\frac{\sqrt{1-a_n}}{a_n R_G T_w} \xi_{n,r} \xi_{n,i}) \quad (2.18)$$

Where I_0 the modified Bessel function of the first kind and of zeroth order, R_G particular gas constant, T_w temperature of the solid surface wall, ξ_n the molecular velocity relative to surface normal vector, $\vec{\xi}_t$ the sum of the tangential components of velocity [22].

2.5 **Numerical methods**

Different methods have been developed to numerically simulate the rarefied gas flows in nozzles. Some of them can also solve the Boltzmann equation. There are two main techniques for solving the Boltzmann equation, Direct Simulation Monte Carlo (DSMC) and Discrete Velocity Method (DVM). DSMC is a probabilistic method that does not rely on the simplifications introduced by the kinetic models. The DVM is an approximate solution and applies the kinetic models.

The DVM is a deterministic approach widely utilized in the scientific community of rarefied gas dynamics to numerically solve the Boltzmann equation and kinetic model equations [10]. The method involves discretizing velocity and space variables using a selected set of discrete velocities and applying a consistent finite difference scheme, respectively. Subsequently, the collision integral term is approximated using an appropriate quadrature, and then the resulting system of equations is solved iteratively. It should be noted that the number of iterations increases rapidly as the Knudsen number decreases, although valid results are obtained across all ranges of Knudsen numbers [9].

G. A. Bird[8] introduced the DSMC method as a stochastic or probabilistic strategy for solving the Boltzmann equation. A DSMC simulation is conducted in a rarefied area using numerical particles to represent numerous physical particles. The simulation involves calculating the motions and collisions of these particles within each time step. Initially, particle trajectories are computed based on their velocity independent of potential intersections, followed by resolving collisions between neighbouring particles using a stochastic approach. At each time step, particles move based on their velocities, interact with the boundaries, and then undergo indexing. A specific number of collision pairs are chosen in each cell using the no-time-counter (NTC) method. This process is iterated until statistical errors meet acceptable levels. Macroscopic properties like temperature or velocity can be derived through averaging over multiple time steps. An accurate simulation depends on three criteria: ensuring that the time step is shorter than the average time between particle collisions for precise trajectory computation, maintaining spatial resolution at the scale of a

particle's mean free path to accurately determine collision partners, and having a sufficiently high number of particles per cell to minimize statistical scattering (20 particles per cell). The DSMC approach has the capability to replicate non-equilibrium and fluctuating gas flow conditions. By conducting simulations over a significant duration, a steady-state flow field can be derived from this method [24,25]. In general interactions between molecules and collisions with surfaces are computed using probabilistic and phenomenological frameworks. Frequently used collision models encompass the Hard Sphere model, the Variable Hard Sphere model, and the Variable Soft Sphere model [9]. In classical kinetic theory the molecular models were really complex, as approximate physical models. A simpler mathematical model is proposed as the hard sphere model (HS). However, the HS molecular model is not accurate as the overall collision cross-section does not rely on the relative velocity of the particle pair engaged in the collision process. G. A. Bird proposed the variable hard sphere (VHS model) that combines the simplicity of the hard sphere model with an improved accuracy. The VHS model can be regarded as a phenomenological model. The attainment of realistic transport properties at the macroscopic level is given priority over the employment of more realistic molecular potentials at the microscopic level [8,26]. An alternative molecular model is the variable soft sphere model (VSS) from K. Koura and H. Matsumoto [27]. The VSS model takes into account anisotropic scattering after collisions. Gas flow in micro-channels is typically characterized by low velocity and operation at around atmospheric pressure. This presents challenges when attempting to extract macroscopic fields like temperature and velocity from DSMC simulations, as the thermal velocities of the particles are significantly higher than the macroscopic velocity. Consequently, recovering the macroscopic velocity becomes statistically challenging, necessitating a large sample size to reduce errors to an acceptable level. Simulations involving very low velocities ($Ma < 0.1$) may be impractical due to exceedingly large required sample sizes [28,29].

The primary method employed in this study was the DSMC computational approach using the Variable Hard Sphere model.

3. Chapter 3: DSMC Method

3.1 Introduction

This chapter offers a more detailed description of the Direct Simulation Monte Carlo (DSMC) [8,30,31]. Unlike traditional continuum-based methods, DSMC excels in capturing the molecular interactions and collisions that become important when gas particles are separated by large distances. Using statistical sampling and Monte Carlo methods, DSMC offers a powerful solution for modelling the dynamics of non-equilibrium gases, making it an indispensable tool for the investigation of aerodynamics, space science and various engineering applications.

3.2 Main Steps of the DSMC Algorithm

The DSMC algorithm consists of several steps. A flow chart of the DSMC method is shown in Figure 3.1. First, the total number of particles, the time step Δt, and basic parameters such as the rarefaction parameter for the given problem are determined. The next step involves constructing the computational grid, which includes cells and sub-cells, and initializing the particles by randomly distributing them within the grid and assigning them the three components of the molecular velocity ξ. If a collision with the solid walls occurs during particle movement, the new component of the particle's velocity after the collision is calculated based on the gas-wall interaction. The following stage involves locating and updating the particles whose initial spatial coordinates have changed. The next step involves the calculation of molecular collisions. In each spatial cell, the probable number of collisions that will occur within each time step Δt is determined using the Non Time Counter (NTC) [28] scheme. The number of potential particle pairs colliding depends on the number of particles in the cell, the cell volume, and the time step Δt. A random pair of particles belonging to the same cell and sub-cell is selected, and the probability of collision is determined based on their relative speed and effective cross-section. When particles collide, their velocities are updated according to the principles of momentum and energy conservation. Next, the macroscopic quantities of the gas are determined based on the microscopic properties of the particles within each cell's geometric medium. At certain points in the process, there is doubling of the initial particles to reduce statistical errors and aid in distinguishing between the initial and final states. The last step of the algorithm is the termination criterion. As a termination criterion, can be used the test of statistical variance if it is less than a certain number or the stopping of the execution of the program at a certain point in time. If the condition is true then the algorithm is terminated. Otherwise, it returns to the first move of the particles. Finally, upon the verification of the convergence condition, the program is terminated [8,26,31].

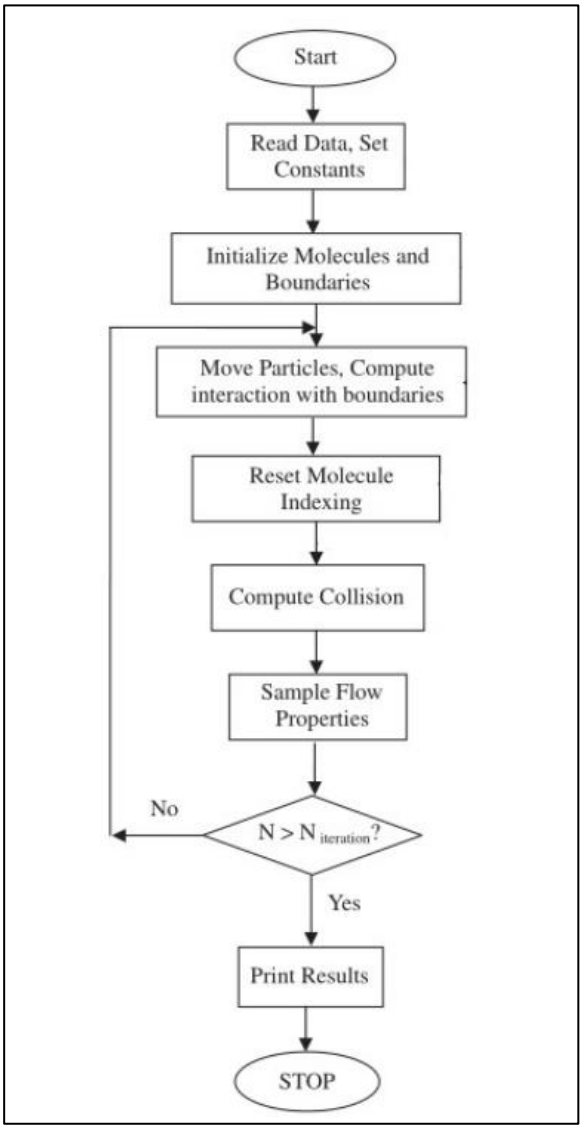

***Figure 3.1**: The standard DSMC procedure [30].*

3.3 **Molecular Description**

In DSMC a vast quantity of simulated particles is used to represent the gas. These particles navigate through the computational space, and their interactions mimic the actions of gas molecules. Each particle acts as a stand-in for a larger number of gas molecules. In DSMC, the simulation typically involves a small fraction of particles compared to the actual number of physical molecules, with each particle representing F_N physical molecules (at least 20 physical molecules for a DSMC particle). The scale of particles employed in simulations can be extensive, particularly in managing large-scale systems, which renders DSMC a method requiring significant computational resources. The key assumption made in DSMC simulations

is that during a small-time interval, molecular motion is considered to be independent of intermolecular collisions. Consequently, each molecule's movement over this period is calculated taking into consideration interactions with flow boundaries. Subsequently, the time advances by one time step and intermolecular collisions are happening. As a result, dynamic action within a gas involves changes in the state variables of individual particles caused by collisions, free movement, and interaction with boundaries [8,26].

3.4 **Random number**

Random numbers are an important aspect of the Monte Carlo method. One must produce a variety of distributions that deviate from the set of random numbers in calculations. While DSMC can generate random values from a range of distributions, it only requires one generator that produces the uniform distribution within the interval. For instance, a random number (R_f) can have values between 0 and 1 and varies each time. Each random number generated during simulation may only be used once. One approach for the use of random numbers is the acceptance-rejection method.

$$\frac{f(x)}{f_{max}} > R_f \tag{3.1}$$

Where f_{max} is the maximum of distribution f. Only the values of x that satisfy this condition are accepted [8,31].

3.5 **Collisions**

At each time step, the particles move freely until a potential collision event is detected. The detection of this event relies on evaluating the positions and velocities of the particles. When a collision is identified, the particles involved undergo a collision event, during which their velocities are updated according to the laws of collision dynamics. This step is fundamental for accurately simulating the molecular interactions within a rarefied gas, setting DSMC apart from continuum methods that neglect such microscale phenomena. The first task in the collision step is to determine the local collision frequency. A well-used method is the No Time Counter scheme, in which the total amount of particle pairs within a cell is selected and then evaluated to determine if a collision will take place [8],

$$N_{Coll} = \frac{N(N-1)F_N(\sigma\xi_r)_{max}\Delta t}{2V_{cell}} \tag{3.2}$$

Where N_{Coll} the number of possible collision pairs, N the current number of particles in cell, F_N is the number of real molecules represented by one DSMC molecule, $(\sigma\xi_r)_{max}$ is the maximum product of the collision cross-section and the relative velocity, V_{cell} is the volume of the collision cell.

The velocities of the particles after the collision are calculated based on Bird's relations [8]. For a monoatomic gas these are formulated as follows:

$$\xi_1^* = \xi + \frac{1}{2}\xi_r \tag{3.3}$$

$$\xi_2^* = \xi_m - \frac{1}{2}\xi_r \tag{3.4}$$

where the velocities ξ_1^* and ξ_2^* are the post-collision vectors, ξ_m is the velocity vector of the centre of mass and ξ_r is the relative velocity of the particles.

3.6 **Macroscopic quantities**

During the DSMC simulation, statistical sampling is often performed to calculate macroscopic quantities such as density, temperature, and velocity. The DSMC method utilizes a particle-based approach to extract the macroscopic properties of gas. This involves collecting data from the simulated particles to estimate these macroscopic properties. These properties are derived from the movement and interactions of the individual particles at the microscopic level. By employing a cell system to sample these macroscopic attributes, they can be utilized for engineering applications. This statistical approach allows researchers to extract meaningful information from the vast amount of particle data generated during the simulation. The accuracy of these sampled macroscopic properties is vital for validating the simulation results against experimental data [32].

The calculation of the numerical density n_j for each cell is defined as:

$$n = \int f d\xi = \frac{m\sum_{k=1}^{S} N(t_k)}{SV'_{cell}} = \frac{mN_T}{SV'_{cell}} \tag{3.5}$$

Where $V'_{cell,}$ is the dimensional volume, S is the number of samples, N are the points of the stochastic system and t is the time.

The macroscopic velocity vector is expressed as:

$$u = \frac{\sum_{k=1}^{S} \sum_{i \in C}^{N} \xi_i \, (t_k)}{N_T} \tag{3.6}$$

The macroscopic velocities for the x, y and z direction are expressed the same.
The dimensional temperature is defined by:

$$T_a = \frac{1}{N_T} \sum_{k=1}^{S} \sum_{i=1}^{N(t_k)} (\xi_{i,a})^2 - (\frac{1}{N_T} \sum_{k=1}^{S} \sum_{i=1}^{N(t_k)} \xi_{i,a})^2 \tag{3.7}$$

Where a is the directions x, y and z and $T = \frac{(T_x + T_y + T_z)}{3}$. The heat flux is defined as:

$$\begin{aligned} q = \frac{1}{N_T} \sum_{k=1}^{S} \sum_{i=1}^{N(t_k)} \xi_{i,x} \left({\xi_{i,x}}^2 + {\xi_{i,y}}^2 + {\xi_{i,z}}^2 \right) - 2u \frac{1}{N_T} \sum_{k=1}^{S} \sum_{i=1}^{N(t_k)} \left({\xi_{i,x}}^2 - u^2 \right) \\ - 2v \frac{1}{N_T} \sum_{k=1}^{S} \sum_{i=1}^{N(t_k)} \left(\xi_{i,x} \xi_{i,y} - uv \right) \\ - 2w \frac{1}{N_T} \sum_{k=1}^{S} \sum_{i=1}^{N(t_k)} \left(\xi_{i,x} \xi_{i,z} - uw \right) \\ - u \frac{1}{N_T} \sum_{k=1}^{S} \sum_{i=1}^{N(t_k)} \xi_{i,x} \left({\xi_{i,x}}^2 + {\xi_{i,y}}^2 + {\xi_{i,z}}^2 \right) \end{aligned} \tag{3.8}$$

The sampling approach plays a crucial role when considering heat flux, as it is essential for transporting heat not only during the free motion of particles but also throughout collision processes. I should be noted that different sampling methods can produce slightly varied results [33].

3.7 **Boundary conditions**

To complete the simulation, DSMC codes must address interactions with solid surfaces or boundaries. Appropriate boundary conditions are implemented to model the reflection, adsorption, or other specified behaviours at these boundaries. The accurate representation of boundary conditions is crucial for obtaining realistic simulations that mimic the physical world. DSMC provides a framework for handling these interactions, making it versatile for a variety of applications, from microscale devices to aerospace engineering. In chapter 2 the two main scattering kernels for gas surface interactions (Maxwell and CLL) were described. The DSMC algorithm used in this thesis is based on the Maxwell diffuse model, where the velocities of

molecules after reflection are not related to their velocities before interaction and follow the Maxwell distribution. In practical situations, gas molecules often have a non-zero flow velocity relative to the surface, creating non-equilibrium conditions near it [8].

3.8 **Description of the model problem**

In this section, the DSMC method is used to analyse a problem of heat transfer in two plates along one dimension. This serves as a simple example to grasp the fundamental concepts of the DSMC method by studying a basic 1D program (a first draft of the code was provided by C. Tantos and it was modified for the calculation of extra moments of macroscopic quantities). The scenario under consideration involves two parallel plates extending infinitely, separated by a distance L while the existing space in between is occupied by fluid. The lower plate maintains a temperature of $T_{down} = T_0 + \Delta T/2$ while the upper one is kept at $T_{up} = T_0 - \Delta T/2$ where T_0 symbolizes the reference temperature. The temperature ratio between the two plates is determined by $\frac{T_{down}}{T_{up}} = (1+\beta)/(1-\beta)$, where β represents $\Delta T/2T_0$.

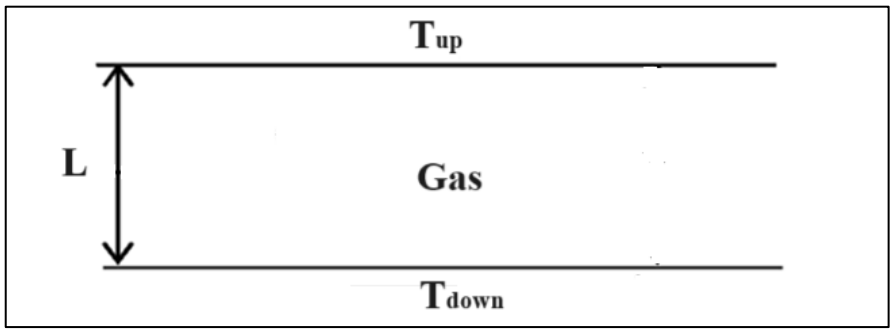

***Figure 3.2**: Model problem set up.*

3.9 **Results of the model problem and sensitivity of the method**

For this model problem, a sensitivity analysis was conducted for the highest value of δ available (because as δ increases the requirements become much higher), and for different values of particles, cells and timestep. The objective is to check the reliability of the three thumb rules: $\Delta x \leq \lambda/3$, $N > 20$ and $\Delta t \leq \tau/3$, where $\tau = \lambda/u_0$ [33].

The findings of heat flux are compared to those of the complete solution with Discrete Velocity Method (DVM) from the paper of S. Pantazis and D. Valougeorgis [34]. The heat flux for this simplified geometry is written as:

$$\widehat{q(y)} = \frac{m}{2} \iiint \xi^2 f d\xi_x d\,\xi_y d\xi_x \tag{3.9}$$

Below, the Table 3-1 presenting the heat flux results from the paper is shown.

***Table 3-1**: Non-linear dimensionless heat fluxes for different values of δ and T_1/T_2 [34].*

δ	$T_1/T_2=(1+\beta)/(1-\beta)$						
	1.01	1.1	1.5	3	7	10	100
0.0	5.643(-3)	5.637(-2)	2.222(-1)	5.058(-1)	6.142(-1)	5.982(-1)	2.830(-1)
1.5(-4)	5.641(-3)	5.636(-2)	2.222(-1)	5.058(-1)	6.142(-1)	5.983(-1)	2.832(-1)
1.5(-1)	5.231(-3)	5.227(-2)	2.064(-1)	4.742(-1)	5.892(-1)	5.818(-1)	3.200(-1)
1.5	3.571(-3)	3.569(-2)	1.414(-1)	3.324(-1)	4.383(-1)	4.485(-1)	3.675(-1)
1.5(+1)	9.917(-4)	9.914(-3)	3.952(-2)	9.675(-2)	1.394(-1)	1.494(-1)	1.643(-1)
1.5(+2)	1.220(-4)	1.218(-3)	4.864(-3)	1.203(-2)	1.773(-2)	1.920(-2)	2.237(-2)

For the initial phase of the sensitivity analysis the comparison is based on the rule $\Delta x \leq \lambda/3$. Also, standard number of 20 particles per cell and timestep $t = 1e-4$ is considered. For all the cases the ratio T_1/T_2 is considered 3. In Table 3-2 the cases for different Δx are shown. According to the rule of thumb the minimum acceptable number of cells for $\delta = 150$ is 500. Based on the results it is evident that the number of cells should be at least 500 for an error value less than 5 %. When the number of cells is less than 400 the error is increased and becomes more than 5%. For increased values of Δx it is observed that the error becomes less than 2 %. The results of the code are also evident in Figure 3.3.

***Table 3-2**: Various cases for $\delta = 150$ and 20 number of particles per cell and timestep $t = 1e-4$.*

Cases	Δx	Particles	Cells	q	q (S. Pantazis)	Error (%)
1	$\ll \lambda/3$	16000	800	0.01224	0.01203	1.77
2	$\leq \lambda/3$	8000	400	0.01260		4.70
3	$\geq \lambda/3$	4000	200	0.01266		5.21
4	$\gg \lambda/3$	800	40	0.01517		26.06

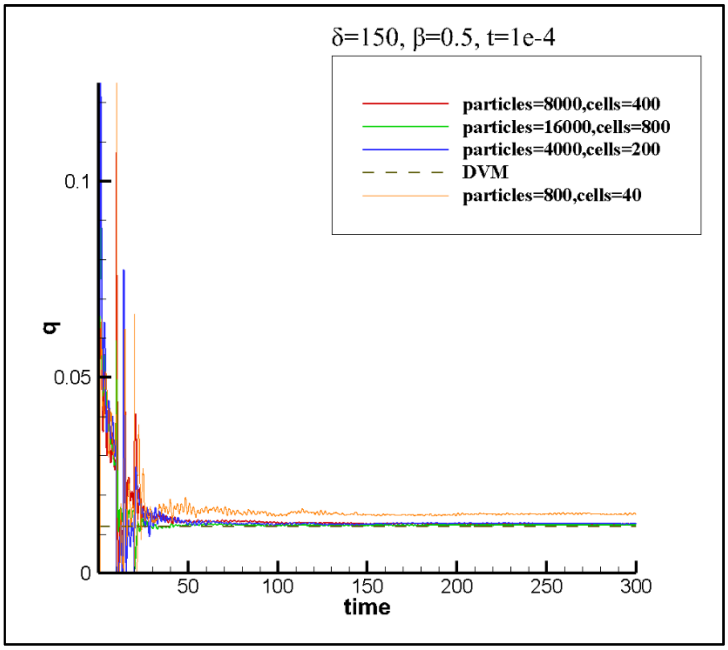

***Figure 3.3**: Graphs of heat flux vs time for different values of Δx.*

The next parameter that will be studied is the number of particles per cell. The cases of 20, 10, 5 and 4 particles per cell will be compared. Based on the results above, where the best case was for 800 cells, the number of cells will be standard at 800. Also, the timestep is $t = 1e - 4$ and the ratio T_1/T_2 is 3. The results are shown in the Table 3-3 and the Figure 3.4. When values of error smaller than 5 % are acceptable it is shown that the least number of particles per cell could be 10.

***Table 3-3**: Various cases for $\delta = 150$ and $cells = 800$ for different number of particles per cell (part/cell).*

Cases	*Part/cell*	Particles	q	q (S. Pantazis)	Error (%)
1	*20*	16000	0.01224	0.01203	1.80
2	10	8000	0.01231		2.37
3	5	4000	0.01253		4.13
4	4	3200	0.01297		7.83

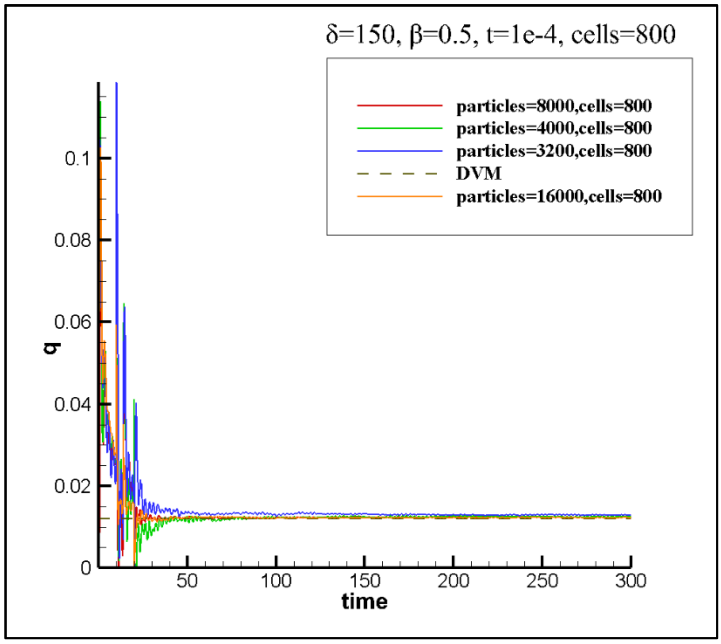

***Figure 3.4**: Graphs of heat flux vs time for different values of particles.*

In the next and final step, a comparison will be made for different time steps ($t = 1e-4$, $t = 1e-3$ and $t = 1e-2$). The ratio T_1/T_2 is 3. Based on the previous results, values of $particles = 16000$ and $cells = 800$ are chosen. The results are shown in Table 3-4 and Figure 3.5. The DSMC solution for $t = 1e-4$ and $t = 1e-3$ is quite close to the DVM solution, in contrast to $t = 1e-2$ which has a slightly larger difference. In addition, as dt decreases, a larger number of iterations are needed to bring the fluid to a steady state.

***Table 3-4**: Various cases for $\delta = 150$, $particles = 16000$ and $cells = 800$ for different timestep.*

Cases	*Timestep*	q	q (S. Pantazis)	Error (%)
1	*1e-4*	0.01224	0.01203	1.72
2	1e-3	0.01180		1.90
3	1e-2	0.009115		27.28

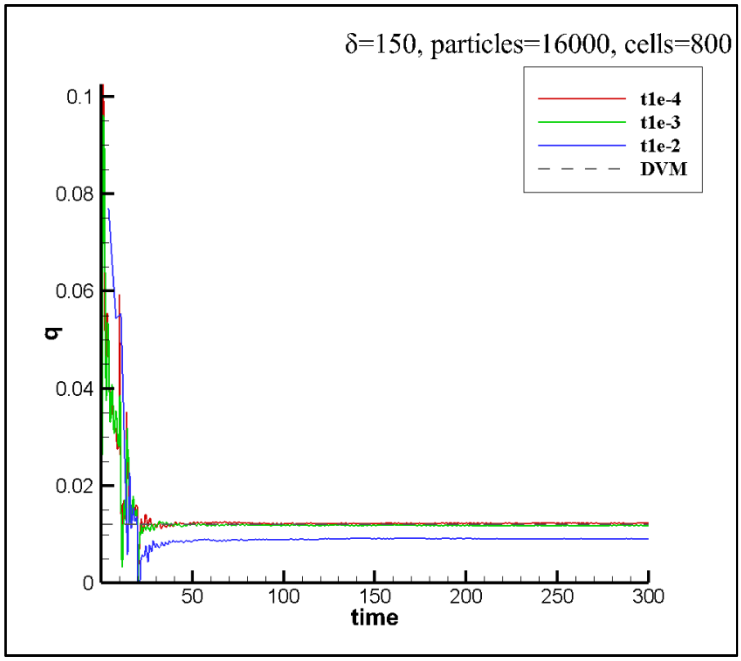

***Figure 3.5**: Diagram of heat flux to time for δ=1.5, β=0.5, particles=8000 and cells=400 for different timestep.*

Upon examination of all the results, it is evident that when the rules are followed the code gives a smaller difference from the DVM solution of the literature [34]. Thus, its validity is also implied. For completeness purposes in Table 3-5 a comparison is also performed for various values of rarefaction parameter and ratio T_1/T_2 is 3, while the three thumb rules are followed. For either of the values of δ the error stays low.

***Table 3-5**: Cases for different values of δ.*

Cases	δ	q	q (S. Pantazis)	Error (%)
1	0.15	0.4741	0.4742	0.021
2	1.5	0.3344	0.3324	0.6
3	*150*	0.01224	0.01203	1.8

4. Chapter 4: Numerical Analysis of Nozzle Performance

4.1 Propulsion Nozzles

Several nozzle designs are currently available, including the converging-diverging nozzle, which is commonly utilized in MEMS and NEMS. Originally invented by Swedish scientist De Laval and now known as the de Laval or converging-diverging nozzle, it features a varying cross-section that can lead to different rarefaction regimes in micro/nanoscale nozzles simultaneously. The shape of the converging section has minimal impact on performance if it allows for easy subsonic flow, while the throat contour is not highly critical to performance and generally accepts any smooth curved shape. Under supersonic flow conditions with certain backpressure values at the exit of the nozzle (or overall pressure differential across the nozzle), a normal shock occurs only in the divergent part of the nozzle. Expansion continues as subsonic flow, after becoming sonic flow at the throat and then returning to supersonic before another shock occurs. Smooth internal wall surfaces throughout are important in minimizing friction and heat transfer. One commonly used design today is the conical nozzle due to its ease of fabrication [2,35–37].

Researchers opt for kinetic-based methods, like direct simulation Monte Carlo, to model fluid flow in small scales encompassing various rarefaction regimes. Existing literature demonstrates extensive utilization of DSMC in forecasting the flow behaviour within micro/nanoscale components such as channels and nozzles [35].

Nozzles play a significant role in regulating the expansion and acceleration of gases under conditions characterized by low molecular density. These intricately designed components have long been essential in industries such as aerospace propulsion, vacuum technology, and manufacturing due to their notable impact on the transition of gas from high-pressure to low-pressure regions while maintaining efficiency. Researchers have been intrigued by the behaviour of gas molecules within nozzles in rarefied regimes where molecular collisions are infrequent. Earlier studies, including G. A. Bird [8], have made fundamental contributions to our understanding of rarefied gas dynamics and laid the groundwork for further research in this field.

A research undertaken by NASA during the initial experimental phase reveals that Reynolds numbers and gas composition have a substantial influence on the functionality of nozzles. The study underscores the significance of boundary-layer effects, particularly at lower Reynolds numbers. Additionally, specific nozzle shapes are recognized as potential factors in enhancing nozzle design for high-performance uses such as satellite propulsion. It is suggested that enhanced predictive models are needed to improve our comprehension and capacity to optimize nozzle performance [38].

A. A. Alexeenko and colleagues [39,40] have conducted an extensive study on the interactions between gas and surfaces in nozzles, providing a deeper

comprehension of wall accommodation coefficients and energy transfer mechanisms under rarefied conditions. Their research highlights the importance of taking into account collision processes and shock wave dynamics when designing and improving nozzles. These observations have significantly improved our capacity to forecast nozzle performance, especially in high-enthalpy flows.

V. A. Titarev et al. [41] investigated the behaviour of rarefied gas flow through a tapered pipe with changing diameter into a vacuum. Their findings suggest that enlarging the pipe diameter leads to higher flow rates regardless of the Knudsen numbers, and it also causes non-linear flow patterns within the pipe.

M. Zhang et al. [42] conducted a study that examined the impact of rarefaction on gas viscosity in a straight channel using the Direct Simulation Monte Carlo method. The numerical investigation showed that variables like wall temperature, rarefaction parameter, and aspect ratio can have a substantial effect on the characteristics of tube flow.

V. Varade et al. [43] carried out an experimental and three-dimensional numerical study that highlighted the importance of viscous shear force in elongated micro-scale channels as a predominant factor contributing to pressure drop. With increasing Knudsen number, convective effects significantly weaken, leading to an increase in the wall friction coefficient.

In the field of nozzle research using the Direct Simulation Monte Carlo approach, a significant number of previous studies has been conducted. Many investigations have focused on studying gas flows within nozzles using DSMC as a dependable simulation tool. However, the current study identifies an important area that has not been extensively explored in existing literature. Specifically aims to provide perspectives by examining the inherent inaccuracies associated with implicit boundary conditions, when combined with DSMC method. Giorgos Tatsios, Dimitris Valougeorgis, and Stefan K. Stefanov [44] conducted a study to investigate the inaccuracies in simulations of straight channels and tubes involving implicit boundary conditions. They obtained findings for the error in the mass flow rate while also applying the end effect correction method. This study aims to test the implicit boundary conditions on diverging channels and compare the results with the literature, as well as with a 1D approach with and without end effects and with a complete solution.

This line of investigation not only enhances understanding of nozzle dynamics but also addresses a crucial aspect that has received limited attention in DSMC-based studies thus far. By carefully analysing the errors related to implicit boundary conditions in DSMC simulations, this chapter aims to bridge this gap and advance discussions about the precision and dependability of such computational methods within the context of nozzle dynamics.

4.2 **Flow Configuration**

A diagram of the studied flow configuration is shown in Figure 4.1. The flow set-up consists of two large reservoirs connected by a diverging channel with length L, width W and height $H(x)$. The height increases linearly in the flow direction. The height of the channel at certain distance from the inlet is defined as $H(x') = [(H_{out} - H_{in})/L]x' + H_{in}$, where H_{in} and H_{out} are the channel height at the inlet and outlet respectively. The width of the channel is assumed to be considerably larger compared to its height ($W \gg H(x')$). The two reservoirs are maintained at different pressures, P_A and P_B, with $P_A > P_B$. At the two reservoirs it is assumed pure isothermal gas flow at T_0. Because of the flow symmetry, only half of the flow domain is considered, ($y' > 0$). Under conditions of equilibrium, a flow is established from the reservoir with high pressure to the one with low pressure. To present the numerical findings more concisely, their dimensionless form is selected. The macroscopic quantities such as the gas number density n, the gas temperature T, the gas velocity vector $\boldsymbol{v}$, are normalized as follows:

$$\rho(x,y) = \frac{n(x,y)}{n_A}, \tau(x,y) = \frac{T(x,y)}{T_0}, \boldsymbol{u}(x,y) = \frac{\boldsymbol{v}(x,y)}{v_0}, \tag{4.1}$$

where $v_0 = \sqrt{2k_B T_0/m}$ is the most probable speed, k_B is the Boltzmann constant and m is the gas molecular mass. The x' and y' coordinates are normalized as $x = x'/H_{in}$ and $y = y'/H_{in}$ respectively.

The state of the gas flow can be described by the following four dimensionless quantities: the reference rarefaction parameter, the dimensionless channel length, the ratio of channel height at the two channel ends and the pressure ratio. The reference rarefaction parameter δ_0 is defined as

$$\delta_0 = \frac{P_A H_{in}}{\mu_0 v_0}, \tag{4.2}$$

where μ_0 is the gas viscosity at the reference temperature T_0. The dimensionless channel length is defined as $\lambda = L/H_{in}$. The ratio of channel height at the two channel ends is H_{out}/H_{in} and the pressure ratio P_B/P_A.

The dimensional gas mass flow rate $\dot{M}$ through the channel is the computational parameter of great importance and its dimensionless form is defined as:

$$M = \frac{\dot{M} v_0 \sqrt{\pi}}{P_A H_{in}}. \tag{4.3}$$

where $\dot{M}_0 = P_A H_{in}/(\sqrt{\pi} v_0)$ is the dimensional mass flow rate in the case of flow through slit ($\lambda = 0$) assuming flow into vacuum ($P_B = 0$) and free molecular flow conditions. The normalization for the mass flow rate has been chosen in order to facilitate comparisons with already existed data in the literature for some limit cases.

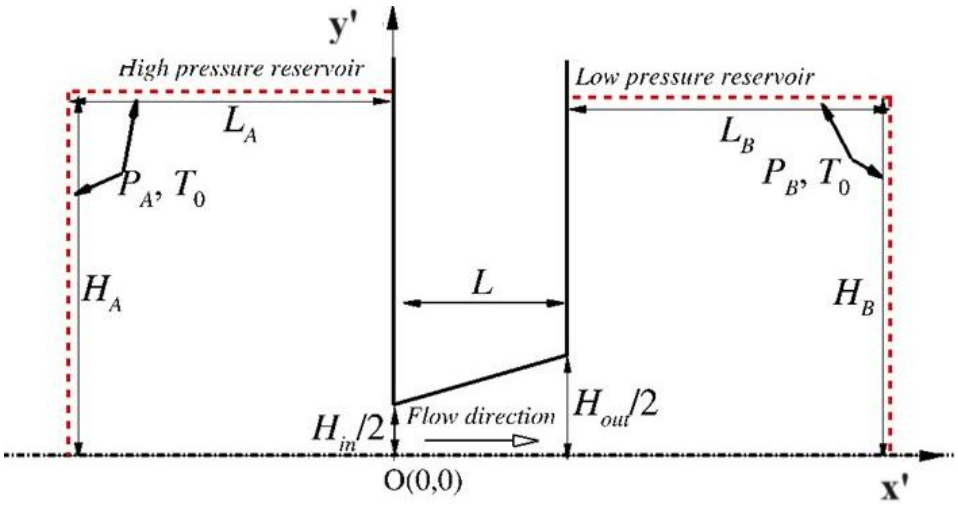

***Figure 4.1**: Flow configuration set up.*

4.3 **Implicit Boundary Conditions**

Microflows frequently operate under specific pressure differentials at the inlet and outlet boundaries. Obtaining velocity distributions at the inlet is often challenging due to experimental constraints. In this problem, implicit boundary conditions [25,42,44–46] are applied to the incoming distributions at the ends of the nozzle. This approach offers the benefit of a small computational domain that includes only the nozzle, whereas achieving a complete solution would require incorporating the reservoirs at the inlet and outlet. In this case $H_A = 0$, $H_B = 0$, $L_A = 0$ and $L_B = 0$. Their theoretical framework presupposes that the flow is locally one-dimensional, inviscid, and adiabatic. These models have been effectively utilized in different scenarios. The implicit boundary conditions are obtained from the Euler equations which describe inviscid flow and have shown to be successful when applied in rarefied flows. This thesis uses an implicit approach for addressing low-speed conditions at the inlet and outlet boundaries in DSMC simulations of microflows under such operational circumstances. Specifically, the particle number fluxes and the velocity components of entering molecules are determined locally from the Maxwellian distribution, where the inlet velocity (i.e. $x = 0$) is:

$$u_{in_j} = u_j + \frac{1 - p_j}{\rho_j \sqrt{2\gamma\tau_j}} \tag{4.4}$$

The inlet number density (ρ_{in}) and temperature (τ_{in}) are obtained from the inlet pressure (p_{in}), where $p = P/P_0$. The reference values are taken as:

$$(\rho_{in})_j = 1 \tag{4.5}$$

$$(\tau_{in})_j = 1 \tag{4.6}$$

The same treatment is also applied for the outlet boundary conditions ($x = L$):

$$\rho_{out\,j} = \rho + \frac{P_{out}/P_{in} - p_j}{\gamma \tau_j} \tag{4.7}$$

$$u_{out\,j} = u_j + \frac{p_j - P_{out}/P_{in}}{\rho_j \sqrt{2\gamma \tau_j}} \tag{4.8}$$

$$\tau_{out\,j} = \frac{P_{out}/P_{in}}{\rho_{out\,j}} \tag{4.9}$$

Where the subscript j is some arbitrary node across the two ends of the channel [44].

The other two boundary conditions on the walls are the maxwell diffuse scattering and the axisymmetric conditions along the symmetry axis ($y = 0$).

4.4 **Fully Developed method**

The cases that occur with the implicit boundary conditions and the DSMC are also analysed using an alternative fully developed approach, which allows for quick estimation of the mass flow rate of the nozzle.

The fully developed method is an 1D approach [47]. This technique computes the mass flow rate through a channel, and the findings will be presented in relation to the reduced mass flow rate as defined below

$$G = \frac{L}{WH_1^2} \sqrt{\frac{2k_B T_1}{m}} \dot{M} \tag{4.10}$$

where L the channel length, m the molecular mass of the gas, k_B is the Boltzmann constant. It is assumed that the channel is sufficiently long enough to neglect the end effects.

The second assumption involves the consideration of small pressure gradients within any cross section of the channel.

$$\xi_p = \frac{H}{P}\frac{dP}{dx},\ |\xi_p| \ll 1 \tag{4.11}$$

where x is the longitudinal coordinate in the flow direction with the origin in the first reservoir. In such a scenario, the mass flow rate within a specific cross section is determined as

$$\dot{M} = HWP\sqrt{\frac{m}{2k_BT}}(-G_p\xi_p) \tag{4.12}$$

where the coefficient G_p depends on the local gas rarefaction parameter δ, defined as

$$\delta = \frac{HP}{\mu(T)}\sqrt{\frac{m}{2k_BT}} \tag{4.13}$$

The values of the coefficient $G_p = G_p(\delta)$ in the case of the gas flow through a rectangular cross section channel for different flow regimes are obtained from the solution of the linearized BGK and S-model kinetic equations, or from the linearized Boltzmann equation for the diffuse or diffuse/specular boundary conditions. From equations (4.11-4.13) the differential equation is:

$$G = \frac{L}{P_1}\left(\frac{H}{H_1}\right)^2(G_P\frac{dP}{dx}(\delta)) \tag{4.14}$$

Equation (4.14) is solved numerically using the following finite difference scheme:

$$P_{i+1} = P_i + \frac{\Delta x}{G_P(\delta_i)}(-\frac{P_1G}{L}\left(\frac{H_1}{H_i}\right)^2) \tag{4.15}$$

where $\Delta x = L/N$ is the grid step in the x direction and $0 \leq i \leq N, P_i, H_i$ are the pressure, and channel height in i grid point, respectively. The rarefaction parameter δ_i becomes:

$$\delta_i = \delta_1 \frac{P_i H_i}{P H_1} \text{ and } \delta_1 = \frac{P_1 H_1}{\mu(T_1)} \sqrt{\frac{m}{2 k_B T_1}} \tag{4.16}$$

Given the inlet pressure, it is possible to determine δ and subsequently G_P can be determined. A random value for G is then hypothesized and the pressures at all nodes are computed. The discovered outlet pressure will be compared with the known pressure. If they vary, these calculations are iterated with a different G. Consequently, upon finding the correct G, the mass flow rate can be ascertained.

A method for correcting the end effect has been suggested to expand the applicability of the infinite channel theory, which describes flows through long channels, to channels of moderate length. The channel's actual length is increased at its two ends by specific increments L_{in} and L_{out}, which are not related to the channel's original length but depend solely on inlet and outlet gas rarefaction parameters, δ_{in} and δ_{out} respectively, with $\delta_{out} = \delta_{in} P_{out}/P_{in}$. The length increments $\Delta L/x$ have been documented based on the gas rarefaction parameter for channel flow [34,47,48].

4.5 Complete Solution

The analysis of the nozzle was also conducted for the complete problem with the reservoirs ($H_A \neq 0$, $H_B \neq 0$, $L_A \neq 0$ and $L_B \neq 0$). The DVM method was used for this solution (a more detailed description is available in the Appendix A). This extra solution was carried out to verify the accuracy of the implicit boundary conditions. It should be noted that if the complete problem is solved with DSMC the results will be similar to those of the DVM solution.

4.6 Parametric Study and Benchmarking

4.6.1 Parametric Analysis

A sensitivity analysis was conducted on rarefied gas flow through a linearly diverging channel into vacuum ($P = 0$), considering pure isothermal conditions. Data for the channel's geometry includes $L/H_{in} = 10$ and $H_{out}/H_{in} = 2$. The comparisons are conducted for the dimensionless mass flow rate M. The parameters under examination are the values of particles, cells timestep and rarefaction parameter. Firstly, the values of $\delta = 0.1$ and $\delta = 10$ are considered for the rarefaction

parameter. For each one of these δ the mass flow rate is studied in comparison with the change in the other three parameters. Each time, the parametric mass flow rate responds to decreased values of cells, particles and timestep.

Table 4-1 shows the results of the sensitivity analysis. It can be seen good agreement between the mass flow rate before and after the change in parameters for either of the three different parameters. Specifically, the error does not exceed the 1 percent for either of the cases.

The equation which is used for the calculation of the error is defined as:

$$Percentage\ Error = \frac{|estimated\ number - actual\ number|}{actual\ number} \times 100 \quad (4.17)$$

***Table 4-1**: Dimensionless flow rate M vs rarefaction parameter δ, for P ratio 0, $H_{out}/H_{in} = 2$ and aspect ratio $L/H_{in} = 10$.*

δ	M (basic)	Changed Parameter	M (for the changed parameter)	Error (%)
0.1	0.5241	cells/2	0.5236	0.099
		particles/2	0.5251	0.185
		timestep/2	0.5240	0.030
10	0.6886	cells/2	0.6874	0.178
		particles/2	0.6925	0.568
		timestep/2	0.6885	0.020

4.6.2 Comparison with available data in literature on diverging channel

In this subsection a comparison is utilised using the findings from the study by O. Sazhin and A. Sazhin [49]. The scenario includes rarefied gas flow through a linearly diverging channel into vacuum ($P = 0$), considering pure isothermal conditions. Data for the channel's geometry includes $L/H_{in} = 10$ and $H_{out}/H_{in} = 2$. The comparisons are conducted for the dimensionless mass flow rate M. The results are shown in Table 4-2. It is evident that the error is high and this defines the present study on the applicability of implicit boundary conditions. Even though there is not good agreement between the two methods for small values of δ, as δ is increased a drastic decrease in error can be seen.

***Table 4-2**: Dimensionless flow rate M vs rarefaction parameter δ, for P ratio 0, $H_{out}/H_{in} = 2$ and aspect ratio $L/H_{in} = 10$.*

δ	M	M (A. Sazhin)	Error (%)
0.1	0.524	0.402	30.473
1	0.479	0.396	20.752
10	0.689	0.593	16.149

4.6.3 Comparison with available data in literature on straight channel

The comparison case in this subsection involves the flow of HS gas in a straight channel of finite length. Pure isothermal flow is considered, while the pressure ratio is 0. The rarefaction parameter δ takes values of 0.1, 1, 10, and 20. Furthermore, data for the channel's geometry includes $L/H_{in} = 1$ and $L/H_{in} = 5$. The comparison is conducted for the dimensionless mass flow rate M.

Table 4-3 shows the comparison between the solution with the implicit boundary conditions and the results from Stylianos Varoutis, Christian Day and Felix Sharipov [14]. Comparing the results for low values of L/H_{in} and δ significant differences from the existing literature are noted. On the other hand, it seems that with an increase in these parameters the differences decrease rapidly. When δ is 10 the error is decreased more than 50 percent when the ratio increases from $L/H_{in} = 1$ to $L/H_{in} = 5$. Considering these results, it would be more efficient to use larger values for these parameters, which could be achieved for the aspect ratio. On the contrary, δ values larger than 10 could not be used because of the computational time at hand.

***Table 4-3**: Dimensionless flow rate M vs rarefaction parameter δ, P ratio and aspect ratio L/H_{in}.*

P ratio	L/H_{in}	δ	M	M (S. Varoutis)	Error (%)
0	1	0.1	1.322	0.698	89.394
		1	1.331	0.767	73.582
		10	1.514	1.04	45.549
		20	1.627	1.15	41.461
	5	0.1	0.450	0.357	26.150
		1	0.426	0.358	18.967
		10	0.551	0.49	12.526
		20	0.709	0.626	13.278

4.7 Results and Discussion

4.7.1 Mass flow rate

Firstly, the results of the dimensionless mass flow rate for L/H_{in} values of 5 and 10, for H_{out}/H_{in} 2 and 5, for δ 1 and 10 and for pressure ratios 0.1 and 0.5 will be commented. Below are the Tables 4-4, 4-5 and 4-6 with the results with implicit boundary conditions in DSMC, fully developed 1D method as in Graur [47] and with the complete solution DVM. Also, the deviations between them have been calculated.

A comparison between the results obtained from using the complete solution and the 1D approach, with and without end effects (as shown in Table 4.4 and Table 4.5 objectively), reveals that when the δ is increased the error is also increased for most of the cases. Additionally, a noticeable decrease in error occurs when end effects are included. The inclusion of end effects leads to more accurate results, explaining the observed differences in errors.

The following analysis entails a comparison between the results obtained using implicit boundaries and the complete solution (as shown in Table 4.6). The complete solution is regarded as the most thorough and precise method when compared to the other two approaches. Upon examination, it is apparent that values obtained with implicit boundaries are larger than those produced by the complete solution. Therefore, it can be stated that the implicit boundaries overestimate the mass flow rate. Moreover, for the vast majority of the results it is observed that the mass flow rate error for these two cases decreases when δ is larger, and is characterized by larger Reynolds numbers which is in accordance to the theoretical basis of the implicit boundary conditions. Additionally, a noticeable increase in error occurs with an increase in H_{out}/H_{in}. Because the nozzle becomes wider and the end effects are more noticeable. Also, when the L/H_{in} ratio increases it is observed that the error decreases due to the reduction of end effects.

In general, when considering the results within the implicit boundaries, it is clear that the mass flow rate increases as δ grows. This can be easily explained by the fact that a higher δ corresponds to greater gas density which results to an increase of the particle-particle collisions and finally to the alignment of particle flow direction with the macroscopic direction of the flow. In addition, an increase in pressure ratio leads to a decrease in mass flow rate across all anticipated scenarios. As the L/H_{in} ratio moves from 2 to 5, there is a consistent reduction in mass flow rate for both pressure ratios due to changes in the nozzle dimensions (elongation and narrowing) leading to decreased flow rates. An examination of the H_{out}/H_{in} ratio reveals that an increase in this ratio is associated with an elevation in mass flow rate, which aligns with expectations since wider nozzles result from this change. Similar observations are found across the other methods, confirming their validity for the qualitative behaviour of the mass flow rate. In general, the increase in the L/H_{in} and in rarefaction parameter leads to decrease of the observed error.

***Table 4-4**: Dimensionless mass flow rate for complete solution and fully developed approach without end effects.*

Dimensionless mass flow rate						
P ratio	L/H_{in}	H_{out}/H_{in}	**δ**	**Complete Solution**	**1D approach without end effects**	**Error (%)**
0.1	5	2	1	0.571	1.019	78.459
			10	0.894	1.489	66.555
		5	1	0.928	2.491	168.427
			10	1.350	4.179	209.556
	10	2	1	0.366	0.509	39.071
			10	0.579	0.744	28.497
		5	1	0.705	1.245	76.596
			10	1.128	2.090	85.284
0.5	5	2	1	0.335	0.551	64.478
			10	0.681	0.985	44.640
		5	1	0.562	1.390	147.331
			10	1.164	2.876	147.079
	10	2	1	0.209	0.275	31.579
			10	0.409	0.493	20.538
		5	1	0.415	0.695	67.470
			10	0.895	1.438	60.670

***Table 4-5**:Dimensionless mass flow rate for complete solution and fully developed approach with end effects.*

Dimensionless mass flow rate						
P ratio	L/H_{in}	H_{out}/H_{in}	**δ**	**Complete Solution**	**1D approach with end effects**	**Error (%)**
0.1	5	2	1	0.571	0.621	8.757
			10	0.894	1.166	30.425
		5	1	0.928	1.657	78.556
			10	1.350	3.376	150.074
	10	2	1	0.366	0.386	5.464
			10	0.579	0.654	12.953
		5	1	0.705	0.995	41.135
			10	1.128	1.867	65.514
0.5	5	2	1	0.335	0.388	15.821
			10	0.681	0.806	18.355
		5	1	0.562	1.017	80.961
			10	1.164	2.353	102.148
	10	2	1	0.209	0.228	9.091
			10	0.409	0.443	8.313
		5	1	0.415	0.587	41.446
			10	0.895	1.294	44.581

***Table 4-6**:Dimensionless mass flow rate for implicit boundary conditions and complete solution.*

Dimensionless mass flow rate						
P ratio	L/H_{in}	H_{out}/H_{in}	**δ**	**Implicit Boundaries**	**Complete Solution**	**Error (%)**
0.1	5	2	1	0.861	0.571	50.613
			10	1.245	0.894	39.296
		5	1	2.369	0.928	155.284
			10	2.998	1.350	122.101
	10	2	1	0.460	0.366	25.773
			10	0.690	0.579	19.136
		5	1	1.195	0.705	69.532
			10	1.929	1.128	70.970
0.5	5	2	1	0.545	0.335	62.780
			10	1.008	0.681	48.114
		5	1	1.449	0.562	157.611
			10	2.976	1.164	155.722
	10	2	1	0.268	0.209	28.139
			10	0.498	0.409	21.637
		5	1	0.692	0.415	66.747
			10	1.698	0.895	89.790

4.7.2 Thrust and Impulse factor

The dimensionless (momentum and total) thrust and Impulse factor were found based on the equations from chapter 1.

Dimensionless Thrust $$f = \frac{F}{P_A H_{in}}. \tag{4.18}$$

Dimensionless Impulse factor $$i_{sp} = \frac{I_{sp}}{\sqrt{\pi} u_o} \tag{4.19}$$

The obtained results for the thrust are shown in Tables 4-7, 4-8 and 4-9. Firstly, by observing the values of the momentum thrust, it can be seen that the two solution methods show the same qualitative behaviour in all cases. With higher δ there is an increase in thrust due to an increase in velocity and mass flow rate. There is also an increase in momentum thrust when the H_{out}/H_{in} ratio increases. There is also a decrease in momentum thrust in cases where the pressure and aspect ratio decreases. It is concluded that momentum thrust exhibits exactly the same behaviour as mass flow rate, as it was expected. Also, as in the mass flow rate the error between implicit

boundary and complete solution decreases with increasing the δ and aspect ratio. Observing the results of the total thrust it appears that the implicit boundaries have exactly the same behaviour as the momentum thrust and therefore the mass flow rate. In contrast the complete solution shows a slight difference. For pressure ratio 0.5, when the δ is increased there is a decrease in total thrust. It is evident that for the total thrust the values of error are increased for $\delta = 10$, which is also the opposite of mass flow rate. This result is probably due to the influence of the outlet pressure. From the comparison of the momentum and total thrust the percentage of momentum thrust that is included in the total thrust can be calculated. The momentum thrust is the 10 % (lowest value) of the total thrust for pressure ratio 0.5, $L/H_{in} = 10$, $H_{out}/H_{in} = 2$ and $\delta = 1$. The momentum thrust is the 100 % (highest value) for pressure ratio 0.1 at $L/H_{in} = 5$, $H_{out}/H_{in} = 5$ and $\delta = 10$. Those values are based on the complete solution.

In Table 4-10 a comparison is conducted for the impulse factor values. As δ increases, the impulse factor also increases, while an expected decrease is observed with increasing aspect ratio based on existing literature [42]. Furthermore, it is concluded that the impulse factor decreases as pressure ratio rises. The difference between the implicit boundary and complete solution diminishes with higher values of δ and L/H_{in}, and lower H_{out}/H_{in} and pressure ratio.

***Table 4-7**: Momentum and total thrust with the implicit boundary conditions.*

P ratio	L/H_{in}	H_{out}/H_{in}	δ	Momentum Thrust	Total Thrust
0.1	5	2	1	0.312	0.390
			10	0.595	0.695
		5	1	1.138	1.225
			10	1.881	1.943
	10	2	1	0.121	0.147
			10	0.258	0.294
		5	1	0.359	0.382
			10	0.884	0.925
0.5	5	2	1	0.047	0.049
			10	0.171	0.177
		5	1	0.150	0.119
			10	0.853	0.837
	10	2	1	0.011	0.020
			10	0.043	0.053
		5	1	0.032	0.037
			10	0.218	0.235

***Table 4-8**: Momentum and total thrust with the complete solution.*

P ratio	L/H_{in}	H_{out}/H_{in}	δ	Momentum Thrust	Total Thrust
0.1	5	2	1	0.131	0.291
			10	0.338	0.448
		5	1	0.185	0.393
			10	0.519	0.519
	10	2	1	0.064	0.176
			10	0.172	0.248
		5	1	0.113	0.293
			10	0.348	0.391
0.5	5	2	1	0.016	0.104
			10	0.075	0.105
		5	1	0.020	0.119
			10	0.102	0.104
	10	2	1	0.007	0.063
			10	0.027	0.053
		5	1	0.011	0.091
			10	0.057	0.072

***Table 4-9**: Error for thrust momentum and total thrust between implicit boundary conditions and complete solution.*

Error					
P ratio	L/H_{in}	H_{out}/H_{in}	**δ**	**Momentum Thrust**	**Total Thrust**
0.1	5	2	1	138.73	33.88
			10	75.99	55.22
		5	1	515.37	211.87
			10	262.33	274.61
	10	2	1	88.09	16.18
			10	50.32	18.37
		5	1	217.82	30.09
			10	154.11	136.24
0.5	5	2	1	185.95	52.61
			10	129.54	68.78
		5	1	644.39	0.11
			10	739.30	705.62
	10	2	1	74.02	67.78
			10	56.94	0.90
		5	1	193.45	58.89
			10	286.27	226.46

***Table 4-10**: Values of Impulse factor.*

P ratio	L/H_{in}	H_{out}/H_{in}	δ	Implicit Boundaries	Complete Solution	Error (%)
0.1	5	2	1	0.362	0.229	58.52
			10	0.478	0.379	26.16
		5	1	0.480	0.199	141.06
			10	0.628	0.385	63.02
	10	2	1	0.263	0.176	49.57
			10	0.375	0.297	26.05
		5	1	0.301	0.160	87.49
			10	0.458	0.309	48.36
0.5	5	2	1	0.086	0.049	75.67
			10	0.170	0.110	54.87
		5	1	0.103	0.036	188.94
			10	0.287	0.087	227.77
	10	2	1	0.043	0.031	35.81
			10	0.085	0.066	28.99
		5	1	0.046	0.026	75.98
			10	0.129	0.063	103.33

4.7.3 Contours of Dimensionless Density, Temperature and Velocity

First, the comparison will be made on the graphs of the dimensionless density for L/H_{in} 5 and 10, for H_{out}/H_{in}= 2 and 5, for $\delta = 1$ and $\delta = 10$ and for pressure ratios 0.1 and 0.5. A comparison will also be made between the method with implicit boundaries and the complete solution. In Figure 4.2 it is observed that the density within the variable cross-section channel decreases as the gas is transferred from high to low pressure, which is expected. This is observed in the results of both methods. Thus, we can say that the qualitative behavior of both methods is the same. In the implicit boundary conditions, it is observed that at the input of the channel the density values are larger than those of the complete solution. This is due to the fact that with the implicit boundaries, we regard the input and output conditions as those of the reservoirs. While in the complete solution the conditions change at the boundaries with the channel and the density is smaller than that of the reservoirs. On the other hand, at the channel output it is observed that the density comparison of the two methods is much better than that of the input. When the ratio of H_{out}/H_{in} decreases and nears the values of a straight channel, it is noted that the representation of implicit boundary conditions at the inlet improves and shows better agreement with the complete solution. This can be rationalized by considering that as H_{out}/H_{in} increases, gas flow moves closer to the limiting case through the slit where there are sharp transitions, leading to implicit boundary conditions diverging from the complete solution. Looking at the different pressure ratios, it seems that the behaviour remains almost the same. At higher pressure ratio at the channel inlet the density comparison seems to be a bit better between the two methods.

In continuation the comparison will be made on the graphs of the dimensionless temperature for L/H_{in} 5 and 10, for H_{out}/H_{in} 2 and 5, for $\delta = 1$ and $\delta = 10$ and for pressure ratios 0.1 and 0.5. The graphs are shown in Figure 4.3. For the small pressure ratio, it is observed that the temperature decreases in all cases for both methods. Thus, the qualitative behaviour remains the same. As a consequence of the energy conservation principle, due to the increase in velocity (which will be shown in the next paragraph) the temperature decreases. It is observed that the implicit boundary conditions show a larger temperature drop towards the channel exit compared to the complete solution. It is also noted that the temperature remains relatively constant in the centre of the nozzle and increases as the gas approaches the walls. The increase in temperature at the walls is expected due to the collisions of the particles with the walls. When the ratio of H_{out}/H_{in} increases, there is a greater decrease in temperature at the centre of the nozzle. This occurs because with an increasing H_{out}/H_{in} ratio, there is a reduction on the wall friction effects. At low H_{out}/H_{in} ratios, the temperature comparison at the nozzle inlet is more consistent between implicit boundary conditions and the complete solution.

In Figure 4.4 a comparison will be performed in terms of the dimensionless velocity for L/H_{in} 5 and 10, for H_{out}/H_{in} 2 and 5, for $\delta = 1$ and $\delta = 1$ and for pressure ratios 0.1 and 0.5 are shown. A comparison will also be made between the method with implicit boundaries and the complete solution. The diagrams in Figure 4.4 show that as the pressure ratio increases (the pressure difference decreases), the velocity decreases, a phenomenon also seen in straight channels. Clearly, when the pressure difference diminishes, the flow slows down. In general, it is noted that velocity tends to increase as the flow approaches the outlet, consistent with observations in straight channels. It is also observed that the velocity values with the implicit boundary conditions compared to the complete solution have a better comparison at the beginning of the nozzle. Towards the exit the velocity appears more increased in the implicit boundary conditions. When δ increases the comparison between the two methods becomes better. This occurs because as the δ increases the Euler assumption becomes more valid (the implicit boundary conditions are due to Euler's assumption on inviscid flow). It has been noted that as the ratio of H_{out}/H_{in} increases, there is an acceleration in flow due to a decrease in wall losses. The velocity follows the well-known parabolic pattern with lower values near the walls and increasing toward the centre.

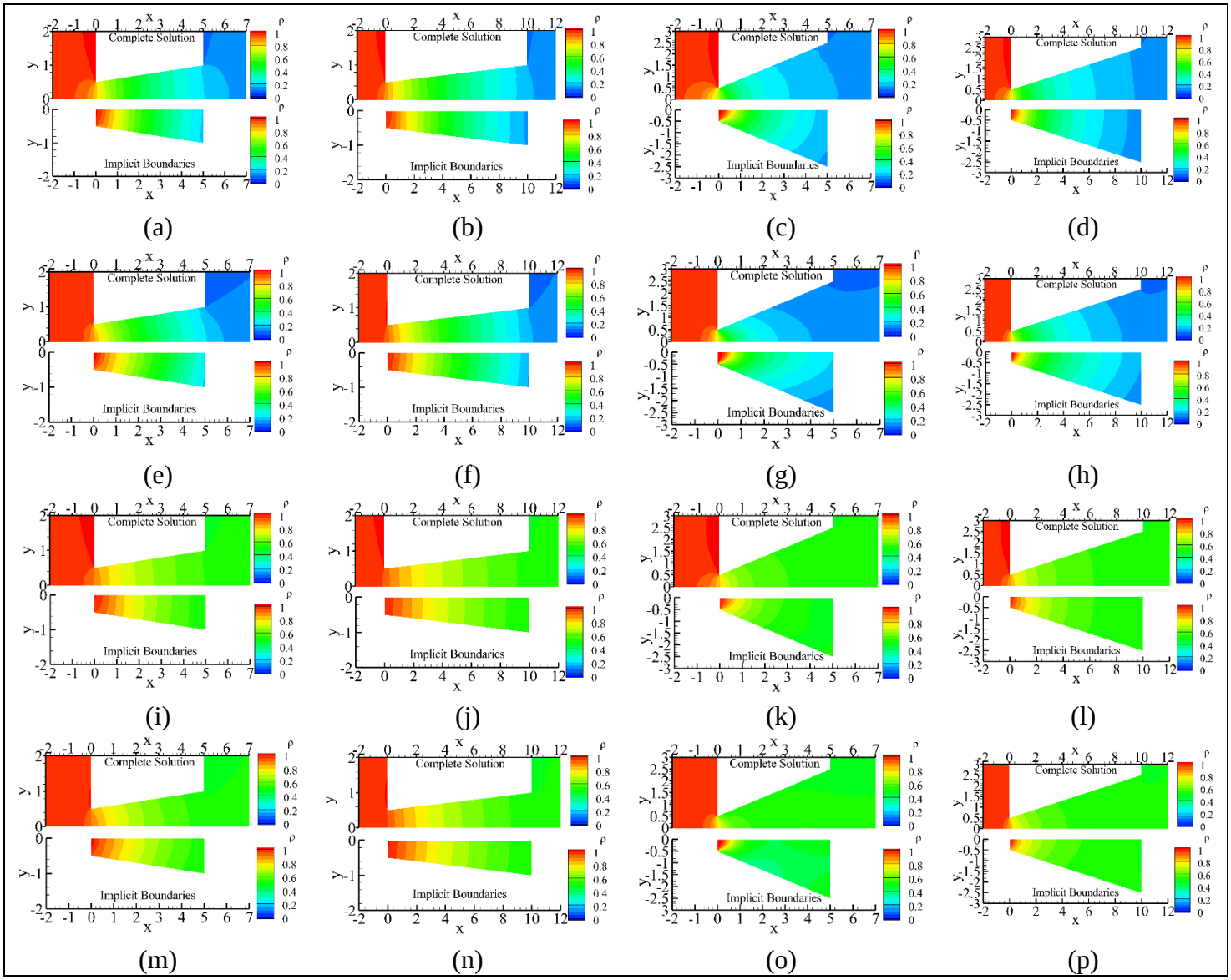

***Figure 4.2**:Density contours for $PR = 0.1$ (a, b, c, d, e, f, g, h) and $PR = 0.5$ (i, j, k, l, m, n, o, p), for $\delta = 1$ (a, b, c, d, I, j ,k, l) and $\delta = 10$ (e, f, g, h, m, n, o, p), for L/H_{in}=5 (a, c, e, g, i, k, m, o) and $L/H_{in} = 10$ (b, d, f, h, j, l, n, p), for $H_{out}/H_{in} = 2$ (a, b, e, f, i, j, m, n) and $H_{out}/H_{in} =$ (c, d, g, h, k, l, o, p).*

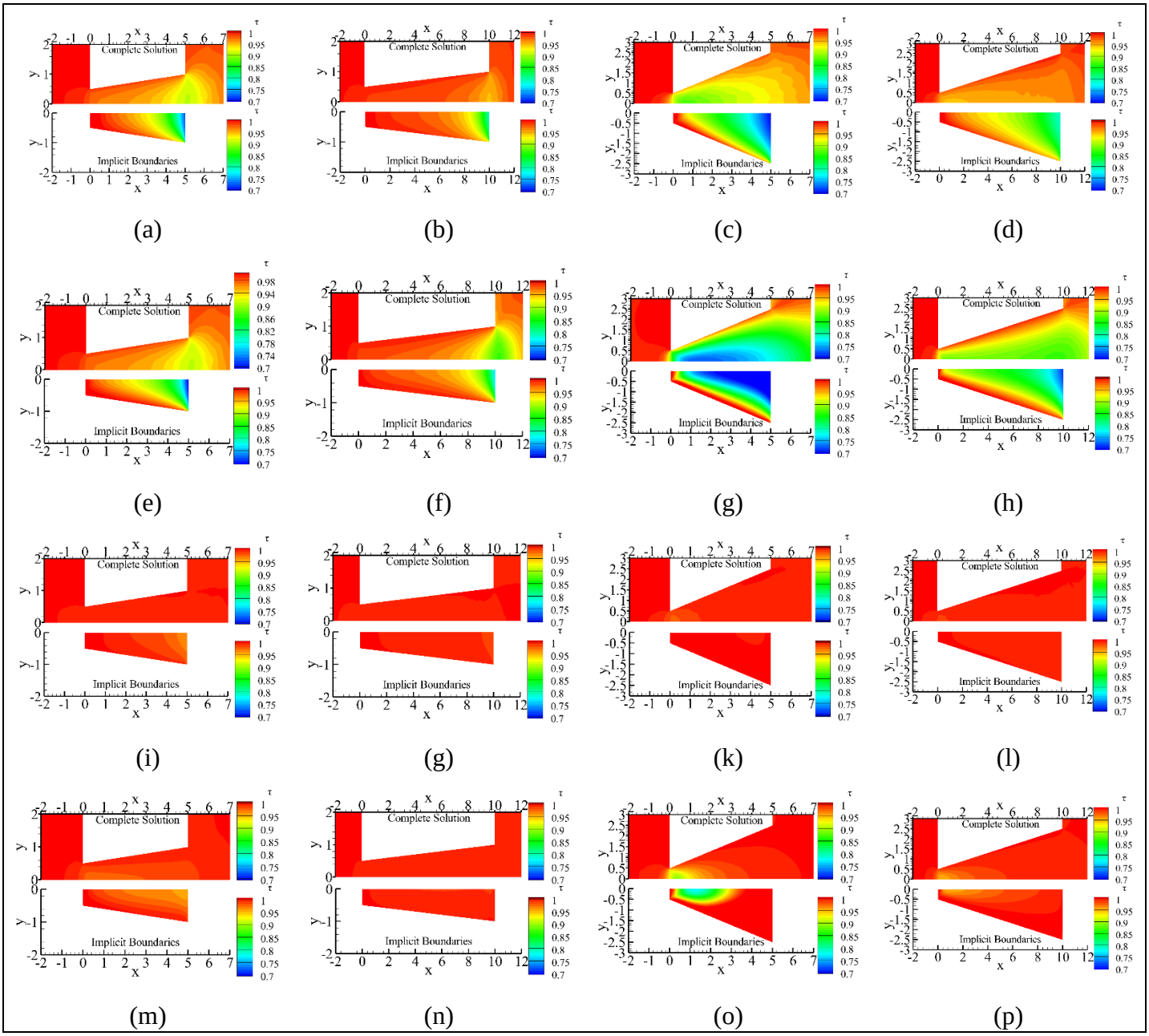

***Figure 4.3**: Temperature contours for $PR = 0.1$ (a, b, c, d, e, f, g, h) and $PR = 0.5$ (i, j, k, l, m, n, o, p), for $\delta = 1$ (a, b, c, d, I, j ,k, l) and $\delta = 10$ (e, f, g, h, m, n, o, p), for L/H_1=5 (a, c, e, g, i, k, m, o) and $L/H_{in} = 10$ (b, d, f, h, j, l, n, p), for $H_{out}/H_{in} = 2$ (a, b, e, f, i, j, m, n) and $H_{out}/H_{in} = 5$ (c, d, g, h, k, l, o, p).*

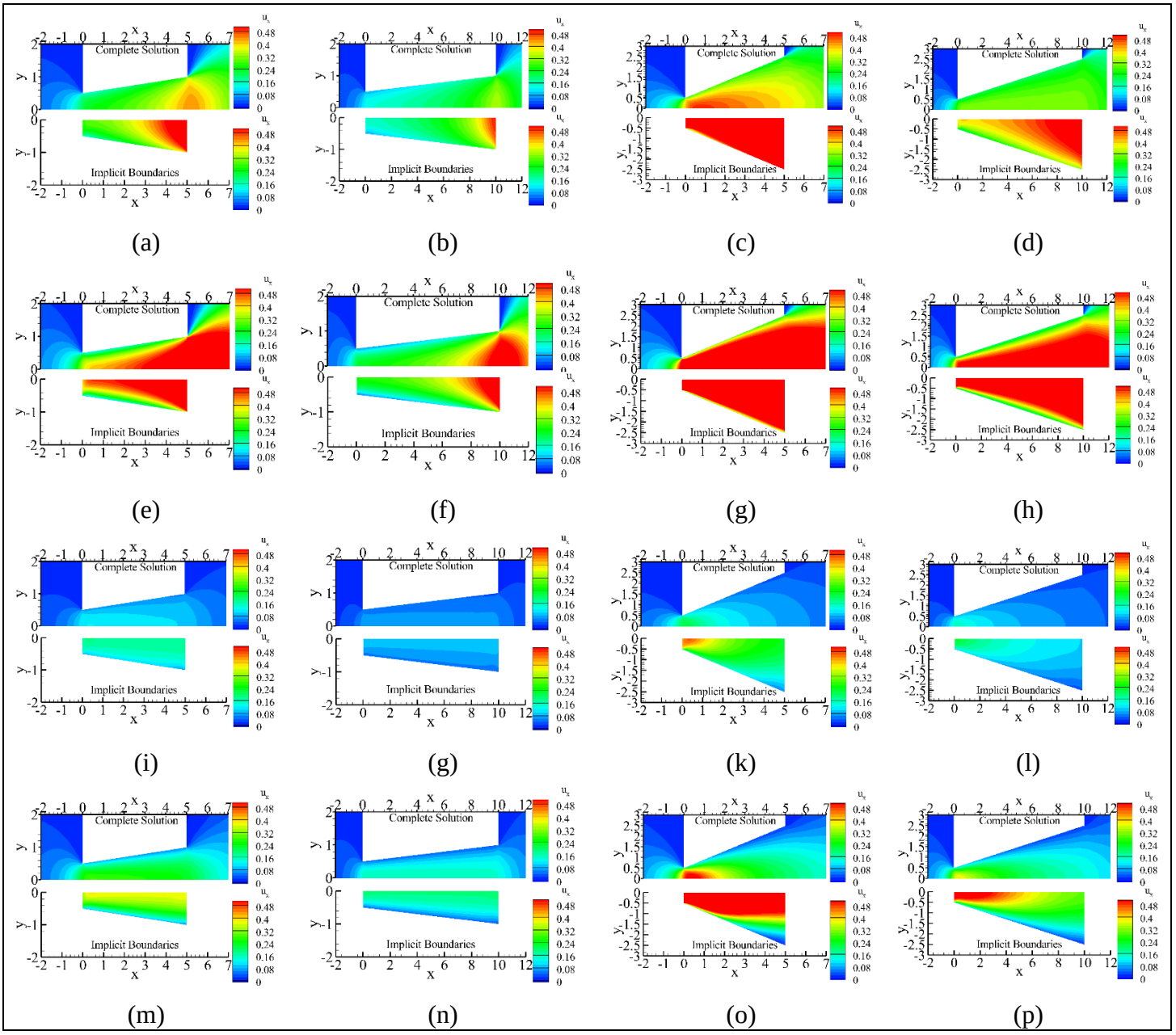

Figure 4.4: *Velocity contours for* $PR = 0.1$ *(a, b, c, d, e, f, g, h) and* $PR = 0.5$ *(i, j, k, l, m, n, o, p), for* $\delta = 1$ *(a, b, c, d, I, j ,k, l) and* $\delta = 10$ *(e, f, g, h, m, n, o, p), for* $L/H_{in} = 5$ *(a, c, e, g, i, k, m, o) and* $L/H_{in} = 10$ *(b, d, f, h, j, l, n, p), for* $H_{out}/H_{in} = 2$ *(a, b, e, f, i, j, m, n) and* $H_{out}/H_{in} = 5$ *(c, d, g, h, k, l, o, p).*

4.7.4 Axial Distributions of Density, Temperature and Velocity

In this paragraph the comparison will be made on the axial diagrams of the dimensionless density for L/H_{in} 5 and 10, for H_{out}/H_{in} 2 and 5, for δ 1 and 10 and for pressure ratios 0.1 and 0.5 (Figure 4.5). A comparison will also be made between the method with implicit boundaries and the complete solution. It is noted that consistency can be observed in the axial distributions across all cases and the two methods. As the H_{out}/H_{in} ratio increases, the profile of the graphs becomes more parabolic as expected for nozzles. Additionally, with increasing this ratio there is a significant decrease in density at the start of the nozzle, followed by a smoother decline at a slower rate. When the H_{out}/H_{in} ratio increases, more significant deviations between the implicit boundary conditions and the complete solution become apparent as a result of increased influence from end effects [44] on the flow. As the pressure ratio increases, there is improved alignment between the two methods. It is observed that when the ratio L/H_{in} increases the comparison of the two methods is improved. This is true due to the reduction in the end effects.

In continuation there are the graphs in Figure 4.6 of the dimensionless temperature for L/H_{in} 5 and 10, for H_{out}/H_{in} 2 and 5, for δ 1 and 10 and for pressure ratios 0.1 and 0.5. It is noted that the comparison of the implicit boundary with the complete solution based on temperature shows a similar sequence to that of the density. It is important to note that at a small H_{out}/H_{in} ratio the flux is nearly isothermal close to 1. While when the ratio increases the values go below 1. The same phenomenon is observed with the L/H_{in} ratio. This occurs mainly due to the increase in velocity.

The axial diagrams of the dimensionless velocity for L/H_{in} 5 and 10, for H_{out}/H_{in} 2 and 5, for δ 1 and 10 and for pressure ratios 0.1 and 0.5 are shown in Figure 4.7. The illustrations indicate that both the implicit boundary and the complete solution exhibit favourable qualitative characteristics across almost all scenarios. In instances of low-pressure ratios and H_{out}/H_{in} ratios, there is an observed rise in channel velocity from the pipeline inlet to outlet. This is justified since as density decreases in the flow direction the velocity increases in order the flow to maintain the mass balance at each cross section. When the pressure ratio increases for small H_{out}/H_{in} ratios, the flow velocity remains nearly constant. This is a characteristic of linear flows under a pressure differential of 1. In this instance, although the pressure ratio is 0.5, there is a notable contrast with a pressure ratio of 0.1. It can be noted that at ratio $P_{out}/P_{in} = 0.5$, as the H_{out}/H_{in} ratio rises, the inlet velocity exceeds that of the outlet. The flow begins to exhibit characteristics typical of flow through a slit. In general, when the H_{out}/H_{in} ratio increases, it is observed that in the implicit boundary and complete solution comparison the deviations increase and the qualitative comparison starts to differ. Like previous cases, the performance of implicit boundary behaviour improves for high L/H_{in} ratios and larger δ values.

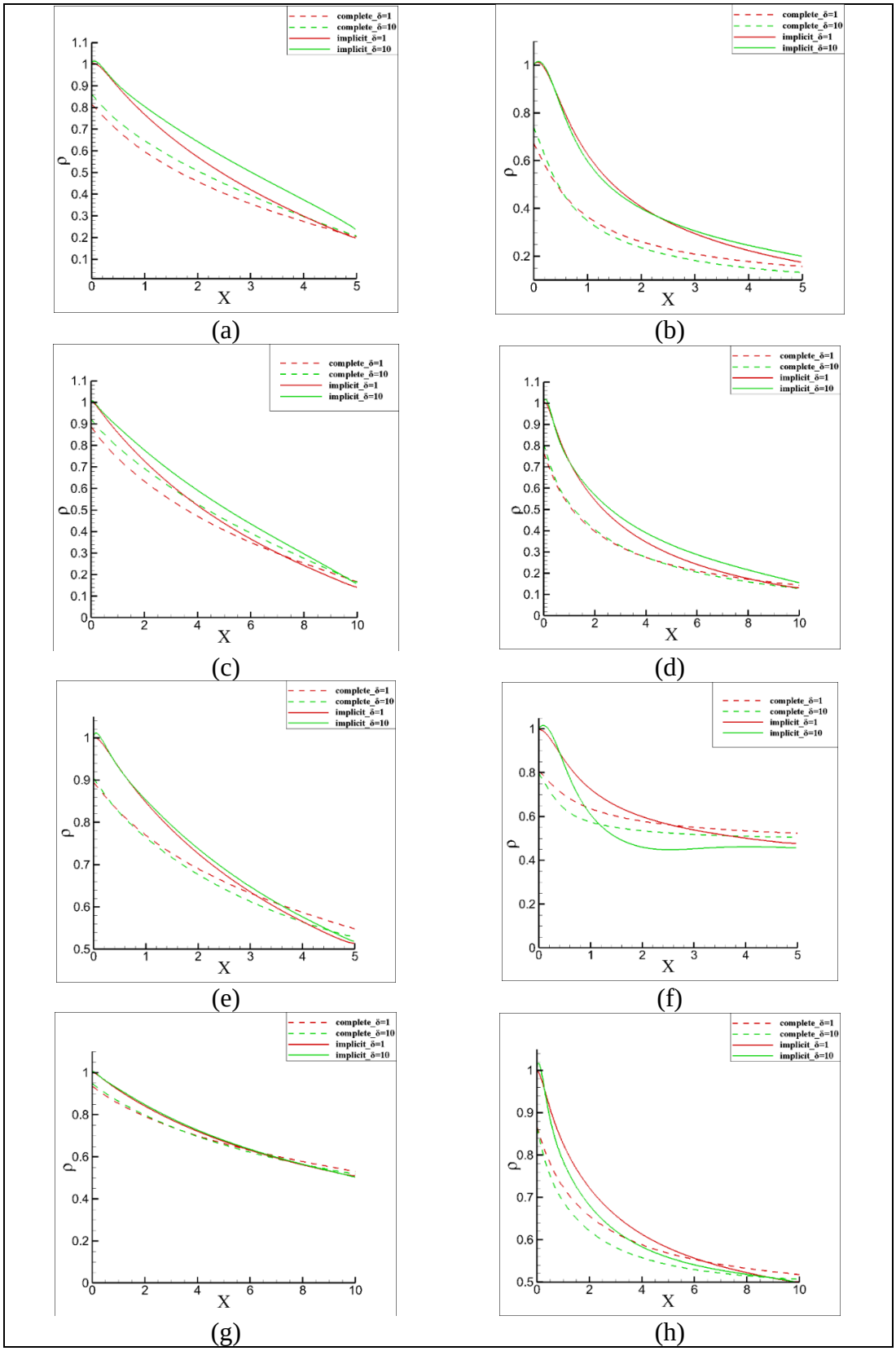

***Figure 4.5**: Axial distributions of density for $PR = 0.1$ (a, b, c, d) and $PR = 0.5$ (e, f, g , h), for $L/H_{in} = 10$ (a, b, e, f) and $L/H_{in} = 10$ (c, d, g, h), for $H_{out}/H_{in} = 2$ (a, c, e, g) and $H_{out}/H_{in} = 5$ (b, d, f, h).*

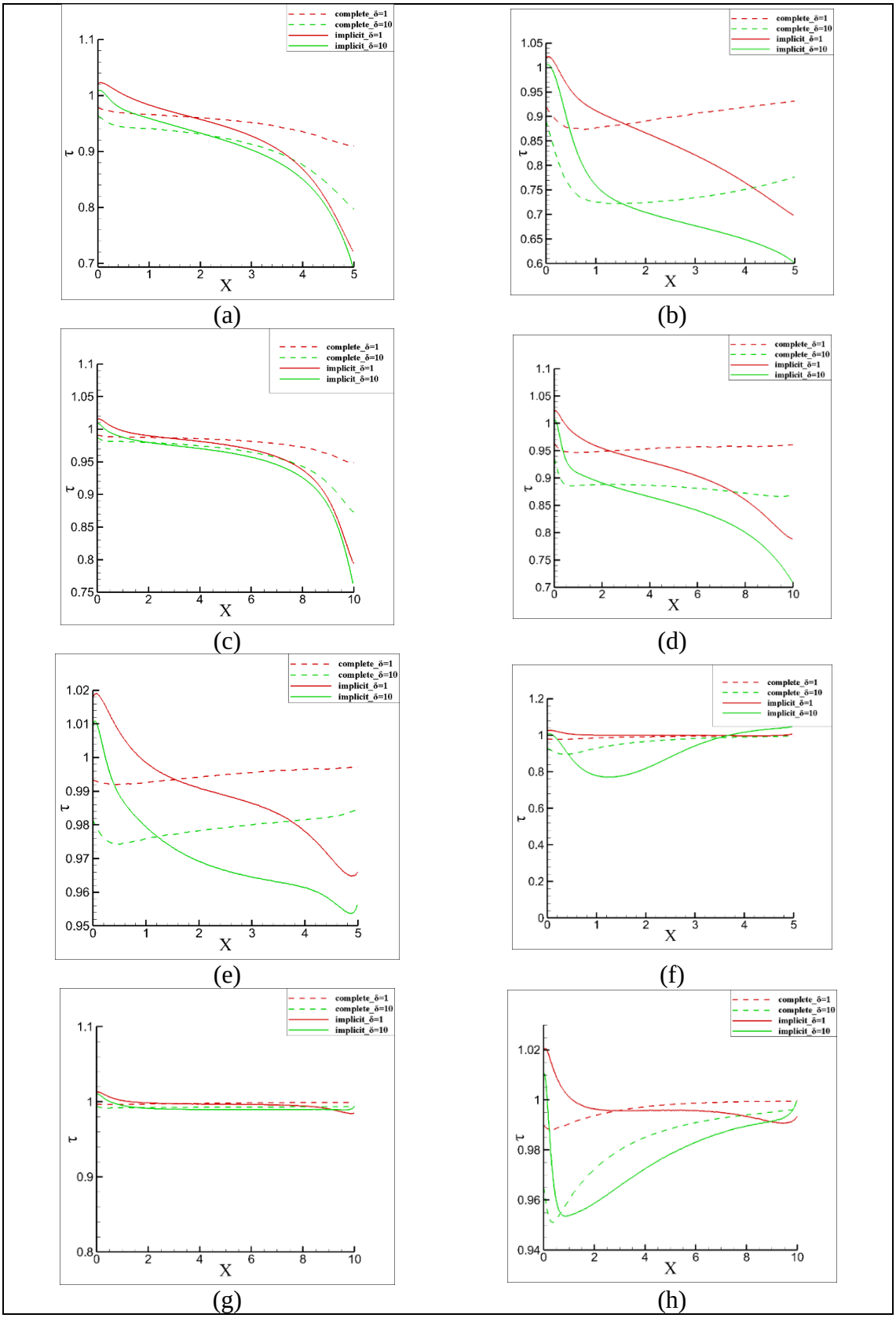

***Figure 4.6**: Axial distributions of temperature for $PR = 0.1$ (a, b, c, d) and $PR = 0.5$ (e, f, g , h), for $L/H_{in} = 5$ (a, b, e, f) and $L/H_{in} = 10$ (c, d, g, h), for $H_{out}/H_{in} = \mathbf{2}$ (a, c, e, g) and $H_{out}/H_{in} = 5$ (b, d, f, h).*

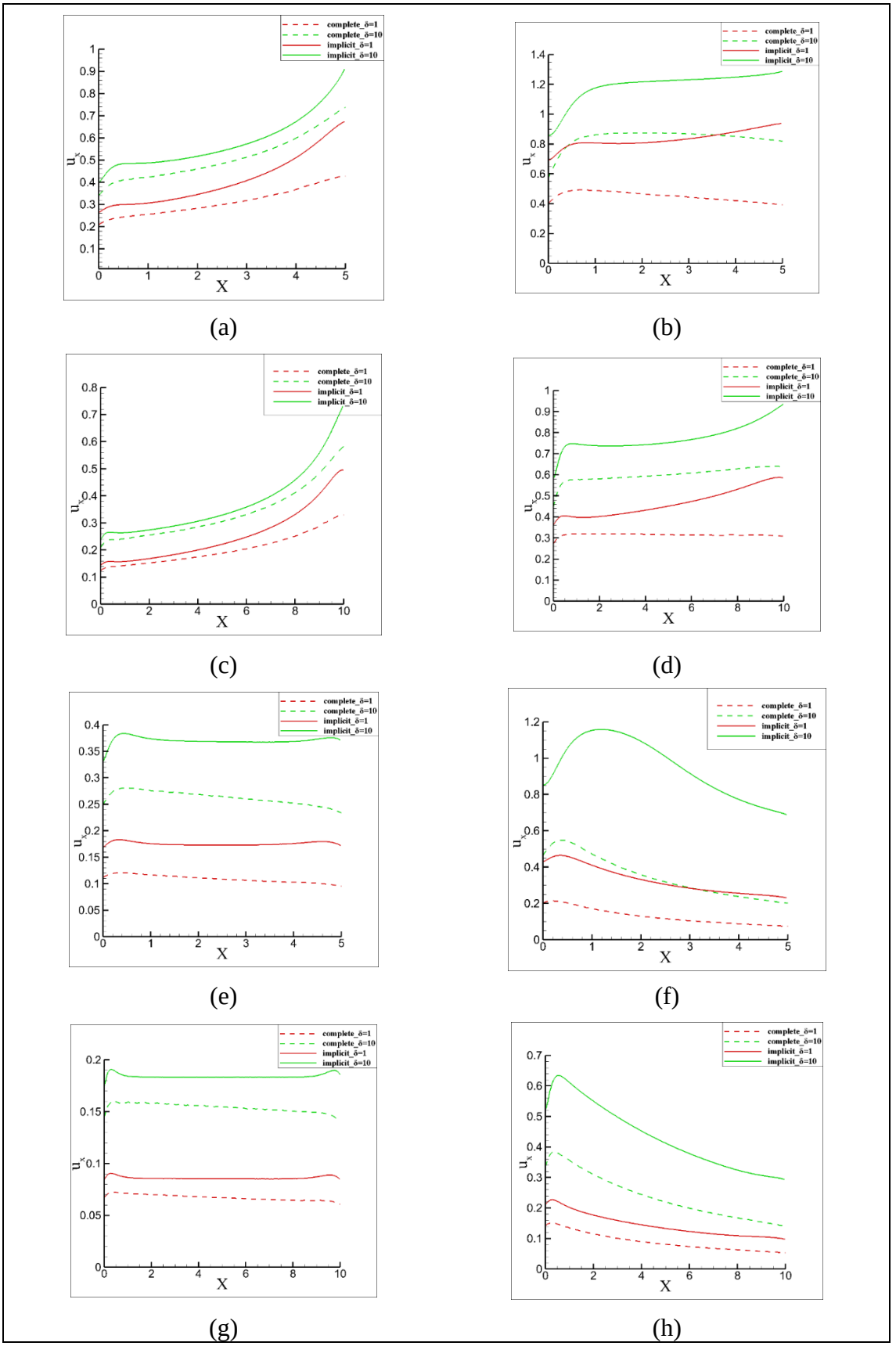

***Figure 4.7**: Axial distributions of velocity for $PR = 0.1$ (a, b, c, d) and $PR = 0.5$ (e, f, g , h), for $L/H_{in} = 5$ (a, b, e, f) and $L/H_{in} = 10$ (c, d, g, h), for $H_{out}/H_{in} = 2$ (a, c, e, g) and $H_{out}/H_{in} = 5$ (b, d, f, h).*

4.7.5 Distributions of Density, Temperature and Velocity along the y-axis

In this paragraph the comparison will be made on the distributions along the y-axis (at the middle of the nozzle) of the dimensionless temperature, density and velocity for L/H_{in} 5 and 10, for H_{out}/H_{in} 2 and 5, for δ 1 and 10 and for pressure ratios 0.1 and 0.5. A comparison will also be made between the method with implicit boundaries and the complete solution.

In Figure 4.8, it can be observed that as L/H_1 increases, the density distribution becomes more uniform. This is reasonable because as the channel length increases, the flow starts to exhibit fully developed flow characteristics. Furthermore, it is evident that in all scenarios, the density results obtained with implicit boundary conditions are higher than those of the complete solution. Consequently, implicit boundaries overestimate density values and similarly do so for velocity values as demonstrated later on. These discrepancies explain why mass flow rate values for implicit boundary conditions surpass those of the complete solution.

In the graphs depicted in Figure 4.9, it is evident that the velocity displays the well-known parabolic profile across all scenarios for both pressure ratios. Furthermore, it can be discerned that even at maximum y, the velocity does not reach zero. This is due to the fact that the methodology also takes into account the slip effects. This means that the gas velocity differs from the zero velocity of the walls. Additionally, an increase in the L/H_{in} ratio results in an accelerated growth of velocity by a factor close to 2.

In Figure 4.10, the diagrams illustrate a decrease in temperature within the channel from the walls to the centre. The highest temperature occurs at the walls as a result of particle-wall interaction, while at the channel's centre, there is a reduction in temperature due to increased fluid velocity and energy conservation purposes. Additionally, it is notable that with higher L/H_{in} ratio, there is a decrease in temperature and the flow becomes more isothermal across the y axis which is in consistency with the fully developed flow characteristics.

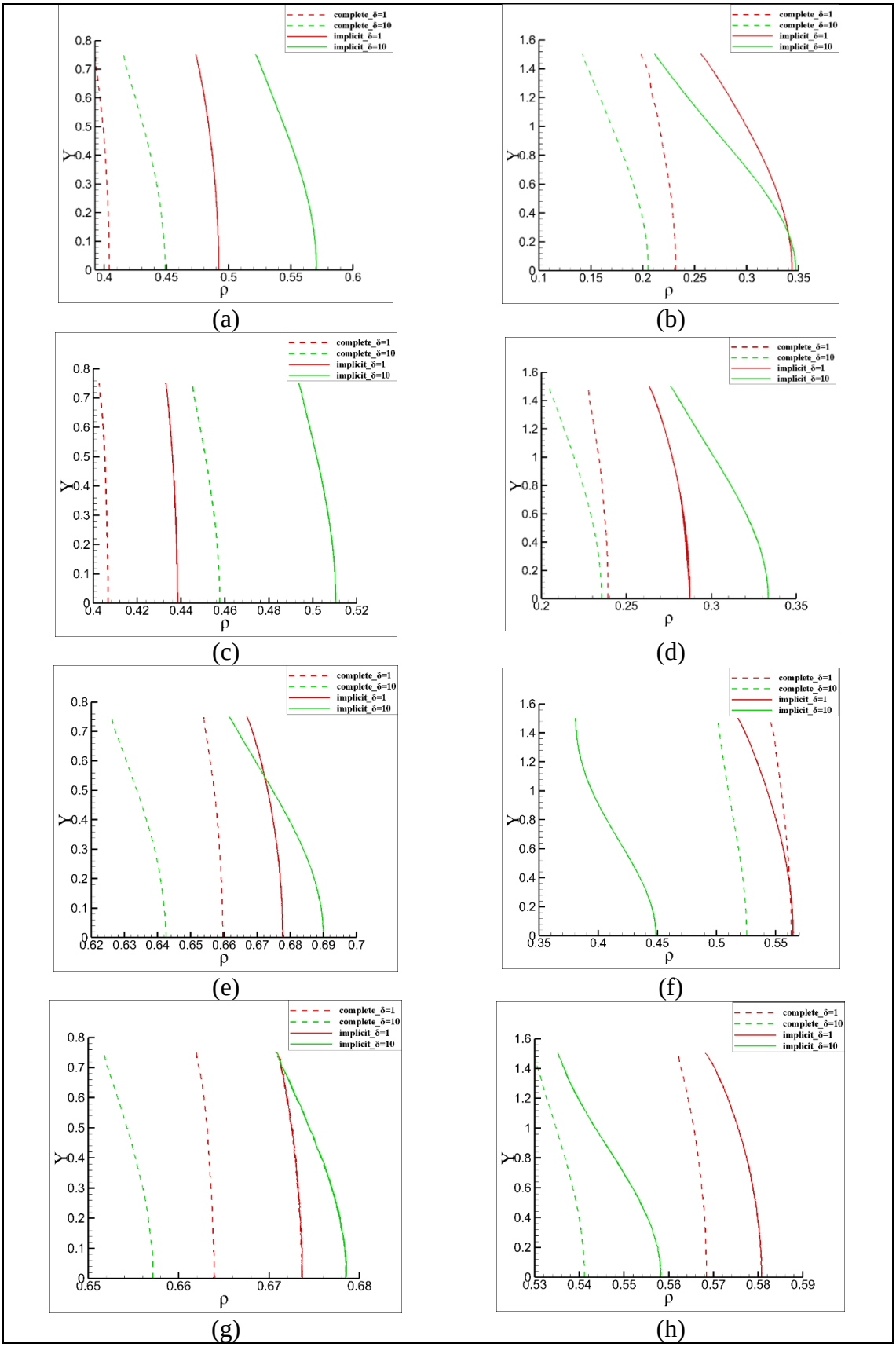

***Figure 4.8**: Perpendicular distributions of density for $PR = 0.1$ (a, b, c, d) and $PR = 0.5$ (e, f, g , h), for $L/H_{in} = 5$ (a, b, e, f) and $L/H_{in} = 10$ (c, d, g, h), for $H_{out}/H_{in} = 2$ (a, c, e, g) and $H_{out}/H_{in} = 5$ (b, d, f, h).*

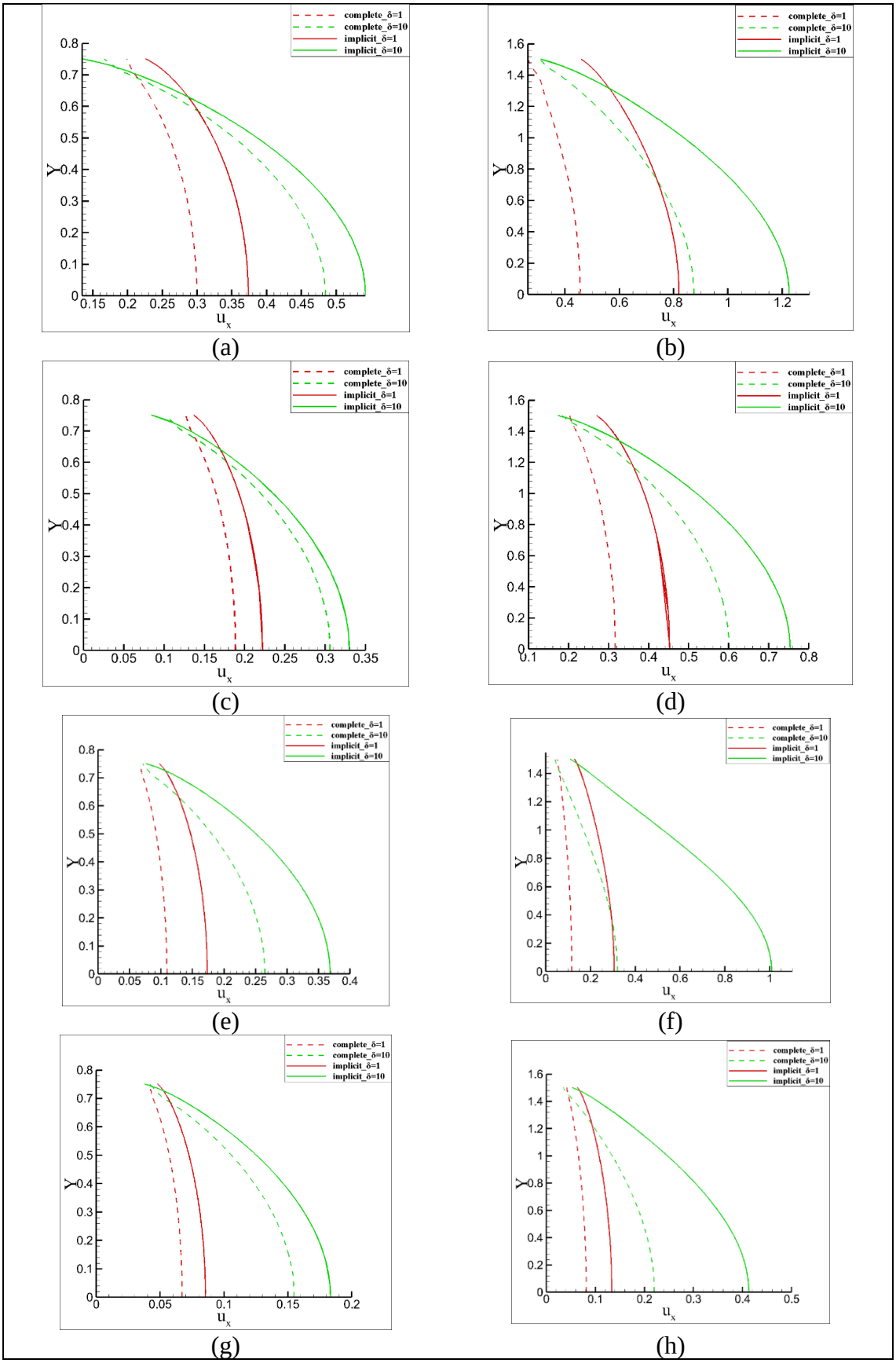

***Figure 4.9**: Perpendicular distributions of velocity for $PR = 0.1$ (a, b, c, d) and $PR = 0.5$ (e, f, g , h), for $L/H_{in} = 5$ (a, b, e, f) and $L/H_{in} = 10$ (c, d, g, h), for $H_{out}/H_{in} = 2$ (a, c, e, g) and H_{out}/H_{in}=5 (b, d, f, h).*

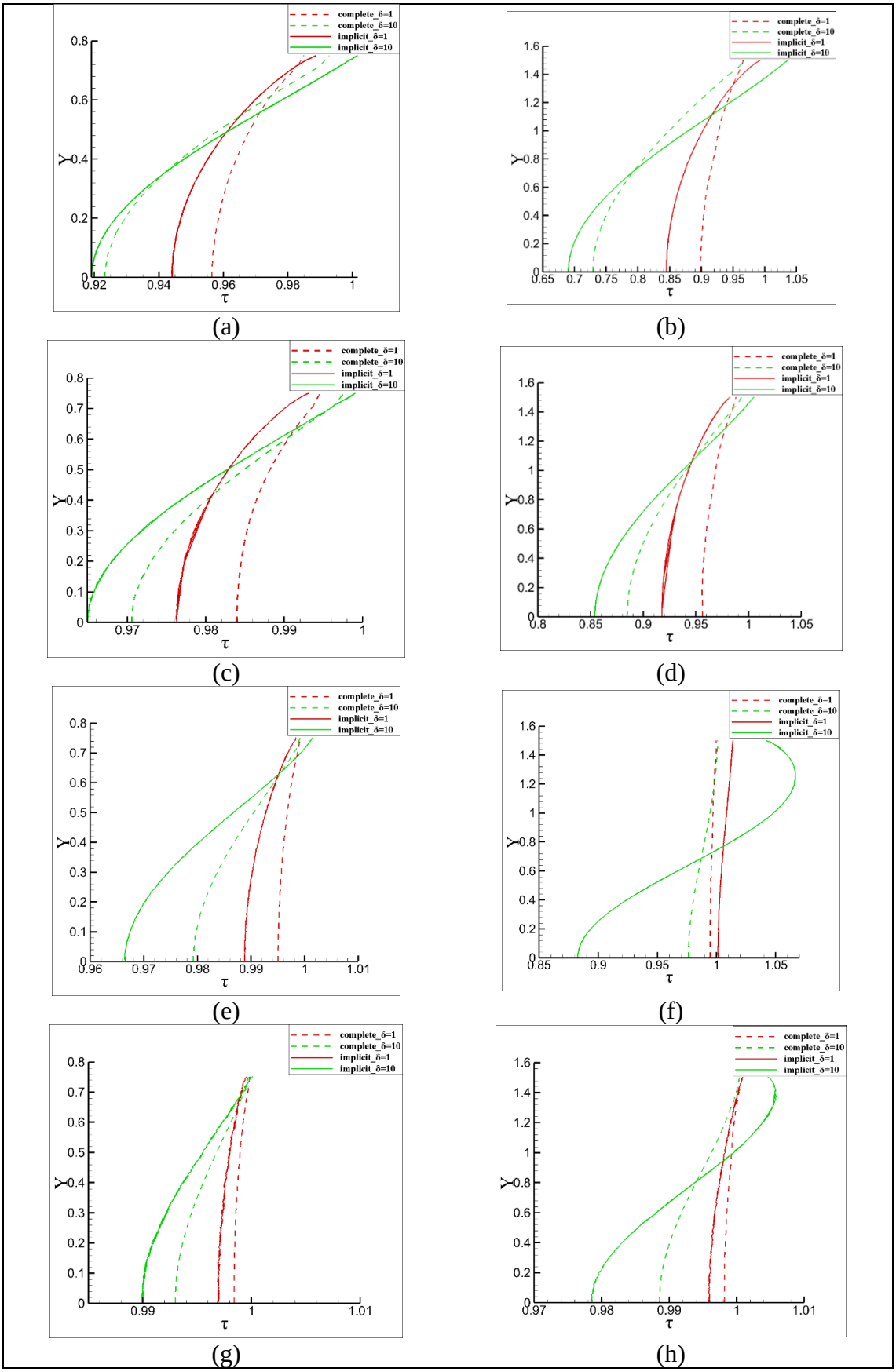

***Figure 4.10**: Perpendicular distributions of temperature for $PR = 0.1$ (a, b, c, d) and $PR = 0.5$ (e, f, g , h), for $L/H_{in} = 5$ (a, b, e, f) and $L/H_{in} = 10$ (c, d, g, h), for H_{out}/H_{in} =2 (a, c, e, g) and H_{out}/H_{in} =5 (b, d, f, h).*

4.7.6 Mach, Knudsen and Reynolds numbers

The Mach, Knudsen and Reynolds numbers are also evaluated for a better understanding of the fluid flow inside the nozzle. The values were calculated at the inlet and outlet of the nozzle. The inlet values were calculated for $x = 0$ and $y = 0.25$, while the outlet values were calculated for $x = 5$ and $x = 10$ (for $L/H_{in} = 5$ and $L/H_{in} = 10$ respectively) and for $y = 0.25$. They were calculated based on the equations in chapter 2. The results are shown in Table 4-11 and Table 4-12 for the implicit boundary conditions and the complete solution respectively.

Observing the Mach number, it appears to exhibit the same qualitative behaviour for both the complete solution and the implicit boundary conditions. With an increase in δ in all cases, there is a decrease in Mach. This behaviour is expected, as there is an increase in velocity for larger δ. Similarly, the increase of Mach when the H_{out}/H_{in} ratio increases can be explained using the same approach. Additionally, there is a decrease in Mach when the L/H_{in} and pressure ratio increase, as velocity decreases. Comparing inlet and outlet values shows an increase in Mach as the velocity also increases. Overall, according to the values of Mach observed across the cases with the complete solution, subsonic flow is observed.

Continuing with the Reynolds number an increase can be seen while the flow moves to the outlet of the nozzle, because of the increased velocity and H. The values of Reynolds are increased when the H_{out}/H_{in} and δ are increased. That is understandable because of the higher velocity.

When examining Knudsen values at low pressure ratios, an increase is observed as the gas moves from the inlet to the outlet of the nozzle. Although there is a rise in H, it appears that the substantial decrease in pressure at the outlet contributes to this increase of Knudsen. Furthermore, with a small pressure difference (P), an increase in H towards the outlet leads to a decrease in Knudsen. Moreover, when considering an increase in the H_{out}/H_{in} ratio, there is a reduction of Knudsen at the outlet due to greater H values. Based on these observations of Knudsen values, it can be inferred that for $\delta = 1$, transition flow occurs, while for $\delta = 10$, slip and transition flow limits are reached.

In general, across all three parameters (Ma, Kn, Re) considered here, when δ and L/H_{in} increase and H_{out}/H_{in} decreases there is an observed decrease in error (Table 4.11).

***Table 4-11**: Mach, Knudsen and Reynolds numbers at the inlet and outlet of the nozzle solved with the implicit boundary conditions.*

				Ma		Kn		Re	
P ratio	L/H_{in}	H_{out}/H_{in}	**δ**	**inlet**	**outlet**	**inlet**	**outlet**	**inlet**	**outlet**
0.1	5	2	1	0.272	0.864	0.887	2.266	0.496	0.617
			10	0.408	1.199	0.088	0.193	7.473	10.054
		5	1	0.736	1.227	0.887	1.016	1.344	1.954
			10	0.942	1.808	0.088	0.090	17.246	32.606
	10	2	1	0.147	0.602	0.887	3.132	0.268	0.311
			10	0.229	0.906	0.088	0.285	4.183	5.144
		5	1	0.377	0.718	0.887	1.349	0.687	0.861
			10	0.626	1.213	0.088	0.115	11.491	17.137
0.5	5	2	1	0.173	0.187	0.888	0.860	0.315	0.351
			10	0.337	0.397	0.088	0.086	6.178	7.517
		5	1	0.453	0.249	0.891	0.370	0.822	1.088
			10	0.935	0.715	0.088	0.039	17.117	29.845
	10	2	1	0.086	0.091	0.886	0.868	0.157	0.170
			10	0.165	0.194	0.088	0.088	3.025	3.585
		5	1	0.220	0.107	0.890	0.354	0.401	0.488
			10	0.553	0.316	0.088	0.036	10.137	14.415

***Table 4-12**:Mach, Knudsen and Reynolds numbers at the inlet and outlet of the nozzle solved with the complete solution.*

				Ma		Kn		Re	
P ratio	L/H_{in}	H_{out}/H_{in}	**δ**	**inlet**	**outlet**	**inlet**	**outlet**	**inlet**	**outlet**
0.1	5	2	1	0.222	0.489	1.081	2.191	0.332	0.361
			10	0.345	0.890	0.104	0.218	5.380	6.591
		5	1	0.448	0.448	1.315	1.124	0.552	0.645
			10	0.643	1.009	0.124	0.135	8.384	12.127
	10	2	1	0.130	0.369	0.997	2.663	0.211	0.224
			10	0.206	0.671	0.096	0.272	3.464	3.991
		5	1	0.293	0.343	1.153	1.230	0.412	0.451
			10	0.475	0.747	0.112	0.137	6.865	8.790
0.5	5	2	1	0.118	0.103	0.988	0.809	0.193	0.206
			10	0.248	0.248	0.098	0.084	4.073	4.762
		5	1	0.219	0.082	1.093	0.338	0.324	0.392
			10	0.497	0.218	0.114	0.035	7.078	10.055
	10	2	1	0.070	0.066	0.945	0.836	0.120	0.127
			10	0.141	0.148	0.093	0.086	2.447	2.808
		5	1	0.151	0.058	1.021	0.342	0.239	0.274
			10	0.344	0.152	0.104	0.035	5.373	7.044

***Table 4-13**: Error (%) for Mach, Knudsen and Reynolds numbers at the inlet and outlet of the nozzle between the implicit boundary conditions and the complete solution.*

				Ma		**Kn**		**Re**	
P ratio	L/H_{in}	H_{out}/H_{in}	**δ**	**inlet**	**outlet**	**inlet**	**outlet**	**inlet**	**outlet**
0.1	5	2	1	22.55	76.71	17.96	3.39	49.38	70.92
			10	18.37	34.81	14.79	11.62	38.92	52.54
		5	1	64.22	173.69	32.57	9.63	143.56	202.84
			10	46.46	79.24	28.80	33.33	105.70	168.87
	10	2	1	12.83	63.18	11.02	17.59	26.80	38.77
			10	10.96	35.09	8.10	4.83	20.75	28.87
		5	1	28.53	109.37	23.03	9.67	66.99	90.91
			10	31.82	62.45	21.25	16.68	67.38	94.97
0.5	5	2	1	46.49	81.56	10.16	6.37	63.05	70.68
			10	36.28	60.50	10.15	1.66	51.67	57.87
		5	1	106.63	203.62	18.47	9.44	153.46	177.43
			10	88.05	228.03	22.24	10.51	141.84	196.83
	10	2	1	22.24	38.99	6.21	3.94	30.33	33.73
			10	17.10	31.02	5.27	2.63	23.61	27.66
		5	1	45.74	84.34	12.88	3.38	67.29	78.31
			10	60.51	107.74	14.92	1.52	88.65	104.64

5. Chapter 5: Conclusions and Future work

5.1 Conclusions

Initially, it was demonstrated that mass flow rate results closely resembled those of the fully developed method without end effects, but differed significantly from the results of the complete solution. Conversely, when end effects were incorporated into 1D approach, the results aligned more closely with those of the complete solution and logically deviated from the implicit ones. Thus, the 1D method with end effects offers a rapid solution with reduced error.

It is important to note that although the analysis was conducted using flat plates of varying cross-sectional shapes (to reduce computational time), it is anticipated that the qualitative behaviour would be similar for nozzles with cylindrical cross-sections.

Generally, it is worth noting that the implicit boundary conditions and the complete solution demonstrate comparable qualitative behaviour across most of the cases.

Moreover, it has been noted that implicit boundary conditions show a much closer resemblance to the complete solution when the H_{out}/H_{in} ratio is small. This implies that implicit boundaries work better when the geometry closely resembles a straight channel. Also, from the findings, it can be inferred that the implicit boundary conditions provide a more accurate approximation of flow at increased δ and a large L/H_{in} ratio. This aligns with the Knudsen number, where smaller Knudsen values favour the use of implicit boundary conditions for better approximation.

These considerations are important when conducting studies on nozzles, to minimize errors and achieve accurate results for nozzle operation and efficiency.

5.2 Future Work

In consideration of the limited computational time available for this study, the main focus was on studying the behaviour of diverging flat nozzles in an isothermal flow setting, specifically for monoatomic gas. Future research opportunities include exploring flow scenarios involving gas mixtures and delving into their distinct characteristics.

Additionally, analysing converging-diverging nozzles could offer valuable insights into their performance and behaviour. There is also potential for a broader research dimension that focuses on a wider range of flow characteristics, with specific attention to various boundary conditions' influence.

Investigating these aspects would contribute to a more thorough understanding of the intricate dynamics associated with nozzle flows, in order to enhance the operation of micro-propulsion systems.

6. Bibliography

1. Robert L. Bayt Analysis, Fabrication and Testing of a MEMS-Based Micropropulsion System 1999.
2. Sutton, G.P.; Biblarz, O. *Rocket Propulsion Elements*; A Wiley-Interscience publication; 7. ed.; Wiley: New York Weinheim, 2001; ISBN 978-0-471-32642-7.
3. Croteau, T. Micro-Nozzle Simulation and Test for an Electrothermal Plasma Thruster. **2018**.
4. Rezaeiha, A.; Mankavi, F. A Study of the Effect of Input Power on Liquified-Gas Resistojet Performance.
5. Mankavi, F.; Rezaeiha, A. Design and Development of a Low Power Laboratory Resistojet.
6. Lawrence, C.T.J. Research into Resistojet Rockets for Small Satellite Applications.
7. Chambre, P.A. *Flow of Rarefied Gases*; Princeton University Press, 2017; ISBN 978-1-4008-8580-0.
8. G. A. Bird *Molecular Gas Dynamics and the Direct Simulation of Gas Flows*; Oxford Science Publications: Oxford, 1994;
9. Τάντος, Χ.; Tantos, C. Effect of Rotational and Vibrational Degrees of Freedom in Polyatomic Gas Heat Transfer, Flow and Adsorption Processes Far from Local Equilibrium, Πανεπιστήμιο Θεσσαλίας, Σχολή Πολυτεχνική, Τμήμα Μηχανολόγων Μηχανικών, 2016.
10. Βασιλειάδης, Ν.; Vasileiadis, N. Gaseous Transport Phenomena in Rarefied Conditions via Deterministic and Stochastic Methods with Applications in Vacuum and Fusion Engineering, Πανεπιστήμιο Θεσσαλίας, Σχολή Πολυτεχνική, Τμήμα Μηχανολόγων Μηχανικών, 2021.
11. La Torre, F.; Kenjeres, S.; Kleijn, C.R.; Moerel, J.-L.P.A. Evaluation of Micronozzle Performance through DSMC, Navier-Stokes and Coupled DSMC/Navier-Stokes Approaches. In *Computational Science – ICCS 2009*; Allen, G., Nabrzyski, J., Seidel, E., Van Albada, G.D., Dongarra, J., Sloot, P.M.A., Eds.; Lecture Notes in Computer Science; Springer Berlin Heidelberg: Berlin, Heidelberg, 2009; Vol. 5544, pp. 675–684 ISBN 978-3-642-01969-2.
12. Cyril Galitzine On the Accuracy and Efficiency of the Direct Simulation Monte Carlo Method 2014.
13. Compressible Flow. In *Fluid Mechanics*; Elsevier, 2012; pp. 729–778 ISBN 978-0-12-382100-3.
14. Varoutis, S.; Day, C.; Sharipov, F. Rarefied Gas Flow through Channels of Finite Length at Various Pressure Ratios. *Vacuum* **2012**, *86*, 1952–1959, doi:10.1016/j.vacuum.2012.04.032.
15. Rapp, B.E. Fluids. In *Microfluidics: Modelling, Mechanics and Mathematics*; Elsevier, 2017; pp. 243–263 ISBN 978-1-4557-3141-1.
16. Menon, E.S. *Gas Pipeline Hydraulics*; 0 ed.; CRC Press, 2005; ISBN 978-0-429-12410-5.
17. Li, Z.-H.; Peng, A.-P.; Ma, Q.; Dang, L.-N.; Tang, X.-W.; Sun, X.-Z. Gas-Kinetic Unified Algorithm for Computable Modeling of Boltzmann Equation and Application to Aerothermodynamics for Falling Disintegration of Uncontrolled Tiangong-No.1 Spacecraft. *Adv. Aerodyn.* **2019**, *1*, 4, doi:10.1186/s42774-019-0009-4.
18. Ludwig Boltzmann *Lectures in Gas Theory*; 1964;

19. Bhatnagar, P.L.; Gross, E.P.; Krook, M. A Model for Collision Processes in Gases. I. Small Amplitude Processes in Charged and Neutral One-Component Systems. *Phys. Rev.* **1954**, *94*, 511–525, doi:10.1103/PhysRev.94.511.
20. Shakhov, E.M. Generalization of the Krook Kinetic Relaxation Equation. *Fluid Dyn* **1972**, *3*, 95–96, doi:10.1007/BF01029546.
21. Maxwell J.C. On Stresses in Rarified Gases Arising from Inequalities of Temperature 1879.
22. Padilla, J.F.; Boyd, I.D. Assessment of Gas-Surface Interaction Models in DSMC Analysis of Rarefied Hypersonic Flow.
23. Cercignani, C.; Lampis, M. Kinetic Models for Gas-Surface Interactions. *Transport Theory and Statistical Physics* **1971**, *1*, 101–114, doi:10.1080/00411457108231440.
24. V. CHARTON; J. LABAUNE High Altitude Rocket Reactive Jet Flow Simulations with a Hybrid NS-DSMC Methodology. **2022**, 13 pages, doi:10.13009/EUCASS2022-7245.
25. Wang, M.; Li, Z. Simulations for Gas Flows in Microgeometries Using the Direct Simulation Monte Carlo Method. *International Journal of Heat and Fluid Flow* **2004**, *25*, 975–985, doi:10.1016/j.ijheatfluidflow.2004.02.024.
26. Bird, G.A. *The DSMC Method*; Version 1.2.; G. A. Bird: S.l., 2013; ISBN 978-1-4921-1290-7.
27. Koura, K.; Matsumoto, H. Variable Soft Sphere Molecular Model for Air Species. *Physics of Fluids A: Fluid Dynamics* **1992**, *4*, 1083–1085, doi:10.1063/1.858262.
28. Hadjiconstantinou, N.G.; Garcia, A.L.; Bazant, M.Z.; He, G. Statistical Error in Particle Simulations of Hydrodynamic Phenomena. *Journal of Computational Physics* **2003**, *187*, 274–297, doi:10.1016/S0021-9991(03)00099-8.
29. White, C.; Borg, M.K.; Scanlon, T.J.; Reese, J.M. Accounting for Rotational Non-Equilibrium Effects in Subsonic DSMC Boundary Conditions. *J. Phys.: Conf. Ser.* **2012**, *362*, 012016, doi:10.1088/1742-6596/362/1/012016.
30. Tisovský, T.; Vít, T. Direct Simulation Monte Carlo Method for Gas Flows in Micro-Channels with Bends with Added Curvature. *EPJ Web Conf.* **2017**, *143*, 02131, doi:10.1051/epjconf/201714302131.
31. Kannenberg, K.C. COMPUTATIONAL METHODS FOR THE DIRECT SIMULATION MONTE CARLO TECHNIQUE WITH APPLICATION TO PLUME IMPINGEMENT. **1998**.
32. Palharini, R.C. Atmospheric Reentry Modelling Using an Open-Source DSMC Code.
33. Hernando, M.V. BULGARIAN ACADEMY OF SCIENCES INSTITUTE OF MECHANICS.
34. Pantazis, S.; Valougeorgis, D. HEAT TRANSFER BETWEEN PARALLEL PLATES VIA KINETIC THEORY IN THE WHOLE RANGE OF THE KNUDSEN NUMBER.
35. Darbandi, M.; Roohi, E. Study of Subsonic–Supersonic Gas Flow through Micro/Nanoscale Nozzles Using Unstructured DSMC Solver. *Microfluid Nanofluid* **2011**, *10*, 321–335, doi:10.1007/s10404-010-0671-7.
36. Das, B.D.; Sardar, R.; Sarkar, S.; Manna, N.K. Compressible Flow Through Convergent–Divergent Nozzle. In *Theoretical, Computational, and Experimental Solutions to Thermo-Fluid Systems*; Palanisamy, M., Ramalingam, V., Sivalingam, M., Eds.; Lecture Notes in Mechanical Engineering; Springer Singapore: Singapore, 2021; pp. 345–353 ISBN 978-981-334-164-7.

37. Dettleff, G. Plume Flow and Plume Impingement in Space Technology. *Progress in Aerospace Sciences* **1991**, *28*, 1–71, doi:10.1016/0376-0421(91)90008-R.
38. Grisnik, S.; Smith, T.; Saltz, L. Experimental Study of Low Reynolds Number Nozzles. In Proceedings of the 19th International Electric Propulsion Conference; American Institute of Aeronautics and Astronautics: Colorado Springs,CO,U.S.A., May 11 1987.
39. Alexeenko, A.A.; Levin, D.A.; Gimelshein, S.F.; Collins, R.; Markelov, G.N. Numerical Simulation of High-Temperature Gas Flows in a Millimeter-Scale Thruster.
40. Alexeenko, A.A.; Fedosov, D.A.; Gimelshein, S.F.; Levin, D.A.; Collins, R.J. Transient Heat Transfer and Gas Flow in a MEMS-Based Thruster. *J. Microelectromech. Syst.* **2006**, *15*, 181–194, doi:10.1109/JMEMS.2005.859203.
41. Titarev, V.A.; Shakhov, E.M.; Utyuzhnikov, S.V. Rarefied Gas Flow through a Diverging Conical Pipe into Vacuum. *Vacuum* **2014**, *101*, 10–17, doi:10.1016/j.vacuum.2013.07.030.
42. Zhang, M.; Day, C.; Varoutis, S.; Cai, G. Rarefied Gas Flow into Vacuum through Short Tubes at Variable Wall Temperatures. *Journal of Vacuum Science & Technology A: Vacuum, Surfaces, and Films* **2017**, *35*, 021604, doi:10.1116/1.4974751.
43. Varade, V.; Duryodhan, V.S.; Agrawal, A.; Pradeep, A.M.; Ebrahimi, A.; Roohi, E. Low Mach Number Slip Flow through Diverging Microchannel. *Computers & Fluids* **2015**, *111*, 46–61, doi:10.1016/j.compfluid.2014.12.024.
44. Tatsios, G.; Valougeorgis, D.; Stefanov, S.K. Reconsideration of the Implicit Boundary Conditions in Pressure Driven Rarefied Gas Flows through Capillaries. *Vacuum* **2019**, *160*, 114–122, doi:10.1016/j.vacuum.2018.10.083.
45. Liou, W.W.; Fang, Y.C. Implicit Boundary Conditions for Direct Simulation Monte Carlo Method in MEMS Flow Predictions. **2000**.
46. Liu, M.; Zhang, X.; Zhang, G.; Chen, Y. Study on Micronozzle Flow and Propulsion Performance Using DSMC and Continuum Methods. *Acta Mech Mech Sinica* **2006**, *22*, 409–416, doi:10.1007/s10409-006-0020-y.
47. Graur, I.; Ho, M.T. Rarefied Gas Flow through a Long Rectangular Channel of Variable Cross Section. *Vacuum* **2014**, *101*, 328–332, doi:10.1016/j.vacuum.2013.07.047.
48. Felix Sharipov Non-Isothermal Gas Flow through Rectangular Microchannels. *Journal of Micromechanics and Microengineering* **1999**, *9*, 394, doi:10.1088/0960-1317/9/4/317.
49. Sazhin, O.; Sazhin, A. Rarefied Gas Flow into Vacuum through Linearly Diverging and Converging Channels. *International Journal of Heat and Mass Transfer* **2023**, *203*, 123842, doi:10.1016/j.ijheatmasstransfer.2022.123842.
50. Graur, I.; Polikarpov, A.Ph.; Sharipov, F. Numerical Modeling of Rarefied Gas Flow through a Slit into Vacuum Based on the Kinetic Equation. *Computers & Fluids* **2011**, *49*, 87–92, doi:10.1016/j.compfluid.2011.05.001.
51. Misdanitis, S.; Pantazis, S.; Valougeorgis, D. Pressure Driven Rarefied Gas Flow through a Slit and an Orifice. *Vacuum* **2012**, *86*, 1701–1708, doi:10.1016/j.vacuum.2012.02.014.
52. Tantos, C.; Valougeorgis, D. Conductive Heat Transfer in Rarefied Binary Gas Mixtures Confined between Parallel Plates Based on Kinetic Modeling. *International Journal of Heat and Mass Transfer* **2018**, *117*, 846–860, doi:10.1016/j.ijheatmasstransfer.2017.10.050.

53. Tantos, C. Polyatomic Thermal Creep Flows through Long Microchannels at Large Temperature Ratios. *Journal of Vacuum Science & Technology A: Vacuum, Surfaces, and Films* **2019**, *37*, 051602, doi:10.1116/1.5111528.
54. Tantos, C.; Varoutis, S.; Day, C. Heat Transfer in Binary Polyatomic Gas Mixtures over the Whole Range of the Gas Rarefaction Based on Kinetic Deterministic Modeling. *Physics of Fluids* **2021**, *33*, 022004, doi:10.1063/5.0033938.
55. Tantos, C.; Litovoli, F; Teichmann, T.; Sarris, I; Day, C. Numerical Study of Rarefied Gas Flow in Diverging Channels of Finite Length at Various Pressure Ratios. *Fluids* **2024**, *9*(3), doi:10.3390/fluids9030078

7. Appendix

7.1 Appendix A: Complete Solution with DVM

In the complete kinetic solution, the computational domain encompasses both the channel region and the reservoir's area. In practical scenarios, since reservoirs can be much larger than channels, it is common to extend the computational domain into the reservoirs in order to minimize computational efforts. This practice continues until a solution independent of these regions' sizes is obtained.

The computational domain is extended by H_A and L_A in the high-pressure reservoir and by H_B and L_B in the low-pressure reservoir.

The flow behaviour is studied based on the Shakhov kinetic model [20]. The Shakhov model recover both the shear viscosity and thermal conductivity simultaneously, while it fulfils all the collision invariants. For the flow problem under question, the Shakhov governing equations in terms of the dimensionless quantities can be written as [50,51]:

$$c_x \frac{\partial}{\partial x}\begin{bmatrix} h \\ g \end{bmatrix} + c_y \frac{\partial}{\partial y}\begin{bmatrix} h \\ g \end{bmatrix} = \delta_0 \rho\, \tau^{1-\omega} \left\{ \begin{bmatrix} h_s \\ g_s \end{bmatrix} - \begin{bmatrix} h \\ g \end{bmatrix} \right\}, \tag{7.1}$$

where $\boldsymbol{c} = (c_x, c_y)$ is the dimensionless molecular velocity vector which in dimensional form reads as $\boldsymbol{\xi} = (c_x v_0, c_y v_0)$, and ω is the viscosity index, with its two limit cases being 0.5 for Hard-Sphere molecules and 1 for Maxwell molecules. The relaxing Shakhov distribution functions h_s, and g_s are read as:

$$\begin{bmatrix} h_s \\ g_s \end{bmatrix} = \begin{bmatrix} \dfrac{\rho}{\pi\tau} \exp\left[\dfrac{-(\boldsymbol{c}-\boldsymbol{u})^2}{\tau}\right] \left\{1 + \dfrac{4}{15\rho\tau^3}\tilde{\boldsymbol{q}}(\boldsymbol{c}-\boldsymbol{u})[(\boldsymbol{c}-\boldsymbol{u})^2 - 2\tau]\right\} \\ \dfrac{\rho}{2\pi} \exp\left[\dfrac{-(\boldsymbol{c}-\boldsymbol{u})^2}{\tau}\right] \left\{1 + \dfrac{4}{15\rho\tau^3}\tilde{\boldsymbol{q}}(\boldsymbol{c}-\boldsymbol{u})[(\boldsymbol{c}-\boldsymbol{u})^2 - \tau]\right\} \end{bmatrix}, \tag{7.2}$$

where $(\boldsymbol{c}-\boldsymbol{u})^2 = (c_x - u_x)^2 + (c_y - u_y)^2$ and $\tilde{\boldsymbol{q}}(\boldsymbol{c}-\boldsymbol{u}) = \tilde{q}_x(c_x - u_x) + \tilde{q}_y(c_y - u_y)$, the dimensionless heat flux. The macroscopic quantities of interest can be calculated as moments of the distribution functions h, and g as:

$$\begin{bmatrix} \rho \\ u_x \\ u_y \\ \tau \\ \tilde{q}_x \\ \tilde{q}_y \end{bmatrix} = \int_{-\infty}^{\infty}\int_{-\infty}^{\infty} \begin{bmatrix} h \\ \dfrac{c_x h}{\tilde{n}} \\ \dfrac{c_y h}{\tilde{n}} \\ \dfrac{2}{3\rho}[(\boldsymbol{c}-\boldsymbol{u})^2 h + g] \\ (c_x - u_x)[(\boldsymbol{c}-\boldsymbol{u})^2 h + g] \\ (c_y - u_y)[(\boldsymbol{c}-\boldsymbol{u})^2 h + g] \end{bmatrix} dc_x dc_y \,. \tag{7.3}$$

A complete kinetic formulation requires the definition of the boundary conditions. In the modelling the particles enter the computational domain following the Maxwellian model at the reservoir conditions. Also, particles enter the computational domain along the open boundary lines in low-pressure reservoir at the corresponding conditions. Diffuse boundary conditions are applied along the solid walls. In addition, symmetry boundary conditions are imposed along the x-axis.

The study of the considered flow set-up involves the solution of a 4D kinetic problem, which is 2D in the velocity space and 2D in the physical space. The system of the two kinetic equations is solved by applying the discrete velocity method (DVM). Nowadays, the deterministic DVM approach is widely acknowledged among researchers as a popular numerical method for solving kinetic equations and representing heat, mass, and momentum transfer phenomena across the full spectrum of gas rarefaction [52–54]. The kinetic solution in physical space is achieved with the use of a non-uniform triangular mesh and the size of the mesh depends on the geometrical characteristics. When the maximum relative difference of the local number density, velocity, and temperature between two successive iteration steps is less than 10^{-12}. it is assumed that convergence has been achieved. Once the simulation stabilizes, the disparity between the dimensionless mass flux values at the inlet and outlet diminishes to below 1 percent. The suitability of the numerical factors was verified through conducting test simulations using an increased quantity of molecular velocity points, (double the number of discrete velocity points) and denser grids (double the number of grid elements), with the maximum deviation in mass flow rate and other macroscopic properties being lower than 1 % [55].